Monthly Notices
of the
ROYAL ASTRONOMICAL SOCIETY

MNRAS **433,** 1114–1132 (2013)
doi:10.1093/mnras/stt794
Advance Access publication 2013 June 3

Evolution and fate of very massive stars

Norhasliza Yusof,[1,2,3]⋆ Raphael Hirschi,[3,4] Georges Meynet,[5] Paul A. Crowther,[6] Sylvia Ekström,[5] Urs Frischknecht,[3,7] Cyril Georgy,[3,8] Hasan Abu Kassim[1,2,9] and Olivier Schnurr[10]

[1] *Department of Physics, Faculty of Science, University of Malaya, 50603 Kuala Lumpur, Malaysia*
[2] *Quantum Science Center, Faculty of Science, University of Malaya, 50603 Kuala Lumpur, Malaysia*
[3] *Astrophysics, Lennard-Jones Laboratories, EPSAM, Keele University, Staffordshire ST5 5BG, UK*
[4] *Kavli Institute for the Physics and Mathematics of the Universe (Kavli IPMU, WPI), University of Tokyo, 5-1-5 Kashiwanoha, Kashiwa 277-8583, Japan*
[5] *Geneva Observatory, Geneva University, CH-1290 Sauverny, Switzerland*
[6] *Department of Physics and Astronomy, University of Sheffield, Hicks Building, Hounsfield Road, Sheffield S3 7RH, UK*
[7] *Department of Physics, University of Basel, Klingelbergstr. 82, CH-4056 Basel, Switzerland*
[8] *Centre de Recherche Astrophysique de Lyon, Ecole Normale Supérieure de Lyon, 46 allée d'Italie, F-69384 Lyon cedex 07, France*
[9] *Institute of Space Science, Universiti Kebangsaan Malaysia, 43600 Bangi, Selangor, Malaysia*
[10] *Leibniz-Institut für Astrophysik Potsdam (AIP), An der Sternwarte 16, G-14482 Potsdam, Germany*

Accepted 2013 May 3. Received 2013 April 24; in original form 2013 February 12

ABSTRACT

There is observational evidence that supports the existence of very massive stars (VMS) in the local universe. First, VMS ($M_{\mathrm{ini}} \lesssim 320\,\mathrm{M}_{\odot}$) have been observed in the Large Magellanic Clouds (LMC). Secondly, there are observed supernovae (SNe) that bear the characteristics of pair creation supernovae (PCSNe, also referred to as pair instability SN) which have VMS as progenitors. The most promising candidate to date is SN 2007bi. In order to investigate the evolution and fate of nearby VMS, we calculated a new grid of models for such objects, for solar, LMC and Small Magellanic Clouds (SMC) metallicities, which covers the initial mass range from 120 to 500 $\mathrm{M}_{\odot}$. Both rotating and non-rotating models were calculated using the GENEVA stellar evolution code and evolved until at least the end of helium burning and for most models until oxygen burning. Since VMS have very large convective cores during the main-sequence phase, their evolution is not so much affected by rotational mixing, but more by mass loss through stellar winds. Their evolution is never far from a homogeneous evolution even without rotational mixing. All the VMS, at all the metallicities studied here, end their life as WC(WO)-type Wolf–Rayet stars. Because of very important mass losses through stellar winds, these stars may have luminosities during the advanced phases of their evolution similar to stars with initial masses between 60 and 120 $\mathrm{M}_{\odot}$. A distinctive feature which may be used to disentangle Wolf–Rayet stars originating from VMS from those originating from lower initial masses would be the enhanced abundances of Ne and Mg at the surface of WC stars. This feature is however not always apparent depending on the history of mass loss. At solar metallicity, none of our models is expected to explode as a PCSN. At the metallicity of the LMC, only stars more massive than 300 $\mathrm{M}_{\odot}$ are expected to explode as PCSNe. At the SMC metallicity, the mass range for the PCSN progenitors is much larger and comprises stars with initial masses between about 100 and 290 $\mathrm{M}_{\odot}$. All VMS in the metallicity range studied here produce either a Type Ib SN or a Type Ic SN but not a Type II SN. We estimate that the progenitor of SN 2007bi, assuming a SMC metallicity, had an initial mass between 160 and 175 $\mathrm{M}_{\odot}$. None of models presented in this grid produces gamma-ray bursts or magnetars. They lose too much angular momentum by mass loss or avoid the formation of a black hole by producing a completely disruptive PCSN.

Key words: stars: evolution – stars: massive – stars: mass-loss.

⋆ E-mail: norhaslizay@um.edu.my

1 INTRODUCTION

In the present work, we call very massive stars (VMS), stars with initial masses superior to 100 $M_{\odot}$. For a long time, the evolution of such stars was considered only in the framework of Population III stars. Indeed, it was expected that, only in metal-free environments, could such massive stars be formed, since the absence of dust, an efficient cooling agent, would prevent a strong fragmentation of the protostellar cloud (Bromm, Coppi & Larson 1999; Abel, Bryan & Norman 2002).[1] It came therefore as a surprise when it was discovered that the most metal-poor low-mass stars, likely formed from a mixture between the ejecta of these Population III stars and pristine interstellar medium (ISM), did not show any signature of the peculiar nucleosynthesis of the VMS (Christlieb et al. 2002; Heger & Woosley 2002; Umeda & Nomoto 2002; Frebel, Aoki & Christlieb 2005). While such observations cannot rule out the existence of these VMS in Population III generations (their nucleosynthetic signature may have been erased by the more important impact of stars in other mass ranges), it seriously questions the importance of such object for understanding the early chemical evolution of galaxies. Ironically, when the importance of VMS in the context of the first stellar generations fades, they appear as potentially interesting objects in the framework of present-day stellar populations.

For a long time, observations favoured a present-day upper mass limit for stars around 150 $M_{\odot}$ (Figer 2005; Oey & Clarke 2005). Recently, however, Crowther et al. (2010) have re-assessed the properties of the brightest members of the R136a star cluster, revealing exceptionally high luminosities. The comparison between main-sequence (MS) evolutionary models for rotating and non-rotating stars and observed spectra resulted in high current ($\leq$265 $M_{\odot}$) and initial ($\leq$320 $M_{\odot}$) masses for these stars.

In addition, the advent of all sky transient surveys – unbiased towards specific nearby massive star-forming galaxies – has produced a population of superluminous supernovae (SLSNe; Gal-Yam 2012), which may have VMS as progenitors. SN 2006gy was the first example of such a supernova for which a pair creation supernova (PCSN) was suspected (Smith et al. 2007), while still stronger evidence was reported by Gal-Yam, Mazzali & Ofek (2009) for SN 2007bi from a metal-poor dwarf galaxy at $z = 0.128$. They derived a core helium mass of 100 $M_{\odot}$ for SN 2007bi, and estimated an initial mass of 200 $M_{\odot}$ for its progenitor, although substantially higher initial masses were inferred by Yoshida & Umeda (2011). Most recently, other SN 2007bi-like examples have been identified: PTF10 nmn (Gal-Yam 2012; Yaron, in preparation) and PS1-11ap (Kotak et al., in preparation), suggesting that VMS and PCSN occur at the current epoch.

The above observations trigger a new interest in the formation, evolution and fate of VMS and in particular stimulate the present study. Our aim is mainly twofold: (1) to provide grids for VMS at three different metallicities with and without rotation. These grids are useful to interpret observations of very luminous objects; (2) to study the evolutionary scenario and the final fate of such objects. We want to address questions such as the kind of stars and of supernova explosion (if any) that VMS produce.

In order to realize these two aims, we calculated a new grid of VMS models at solar ($Z = 0.014$), Large Magellanic Cloud (LMC, $Z = 0.006$) and Small Magellanic Cloud (SMC, $Z = 0.002$) metallicities using the GENEVA stellar evolution code (Eggenberger et al. 2008) including the modifications implemented to follow the advanced stages as described in Hirschi, Meynet & Maeder (2004). This work extends the MS models for VMS presented in Crowther et al. (2010) and complements the low- and high-mass stellar grids at solar metallicity ($Z = 0.014$) calculated by Ekström et al. (2012) and Georgy et al. (2012) as well as their extension to lower metallicities (Eggenberger et al., in preparation; Georgy et al., in preparation).

In Section 2, we present the physical ingredients of the models. The description of the results is given in Section 3. The Wolf–Rayet (WR) stars originating from VMS are discussed in Section 4. The final fates of the VMS are the subject of Section 5. Conclusions and perspectives are given in Section 6.

2 PHYSICAL INGREDIENTS OF THE MODELS

The various input physics parameters are the same as the ones used in the new grids of rotating models published in Ekström et al. (2012), making this grid of VMS consistent with their published grid. We just recall here a few important points.

(i) The initial abundances for the models are listed in Table 1. The mixture of heavy elements (Z) is taken from Asplund, Grevesse & Sauval (2005) except for the Ne abundances adopted from Cunha, Hubeny & Lanz (2006) and the isotopic ratios are taken from Lodders (2003).

(ii) Reaction rates are taken mostly from Nuclear Astrophysics Compilation of Reaction Rates (NACRE; Angulo et al. 1999). The full list of updated rates and a short description of the effects on stellar evolution are presented in Ekström et al. (2012).

(iii) Neutrino energy loss in plasma, pair and photoneutrino process is taken from Itoh et al. (1989, 1996).

(iv) Opacities is taken from OPAL (Iglesias & Rogers 1996) and completed with low temperature opacities from Ferguson et al. (2005) adapted for the high Ne abundance.

(v) For convection, the Schwarzschild criterion is used and a modest overshooting with an overshoot parameter, $d_{\rm over}/H_P = 0.10$, is used for core hydrogen and helium burning only.

(vi) The outer convective zone is treated according to the mixing length theory, using $\alpha_{\rm MLT} = 1.0$. As explained in Ekström et al. (2012, and references therein), $\alpha_{\rm MLT} = l/H_{\rho}$, where l is the mixing length and H_{ρ} the density scale height to avoid an unphysical density inversion in the envelope.

(vii) The treatment of rotation in the GENEVA code has been described in Maeder & Meynet (2012). For horizontal turbulence, we used the diffusion coefficient from Zahn (1992) and for the secular shear turbulence, we used the diffusion coefficient of Maeder (1997).

(viii) Note that the effects due to the creation of electron–positron pairs is not included in the equation of state but this does not affect the conclusions of this paper as discussed below.

Table 1. Hydrogen (^{1}H), helium isotopes (^{3}He, ^{4}He) and metal (Z) mass fractions for the chemical abundances in our models.

	^{1}H	^{3}He	^{4}He	Z
Solar	0.7200	4.414e-5	0.2659	0.014
LMC	0.7381	4.247e-5	0.2559	0.006
SMC	0.7471	4.247e-5	0.2508	0.002

---

[1] Note, however, that the most recent star formation simulations find lower mass stars forming in groups, similarly to present-day star formation (Greif et al. 2010; Stacy, Greif & Bromm 2010).

2.1 Mass loss

Mass loss strongly affects the evolution of VMS as we shall describe below. It is therefore important to understand the different mass-loss prescriptions used and how they relate to each other. In this study, we used the following prescriptions. For MS stars, we used the prescriptions for radiative line driven winds from Vink, de Koter & Lamers (2001), which compare rather well with observations (Crowther et al. 2010; Muijres et al. 2011). For stars in a domain not covered by the Vink et al. prescription, we applied the de Jager, Nieuwenhuijzen & van der Hucht (1988) prescription to models with $\log(T_{\rm eff}) > 3.7$. For $\log(T_{\rm eff}) \leq 3.7$, we performed a linear fit to the data from Sylvester, Skinner & Barlow (1998) and van Loon et al. (1999) (see Crowther 2001). The formula used is given in equation (2.1) in Bennett et al. (2012).

In the calculations, we consider that a star becomes a WR when the surface hydrogen mass fraction, $X_{\rm s}$, becomes inferior to 0.3 and the effective temperature, $\log(T_{\rm eff})$, is greater than 4.0. The mass-loss rate used during the WR phase depends on the WR subtype. For the eWNL phase (when $0.3 > X_{\rm s} > 0.05$), the Gräfener & Hamann (2008) recipe is used (in the validity domain of this prescription, which usually covers most of the eWNL phase). In many cases, the WR mass-loss rate of Gräfener & Hamann (2008) is lower than the rate of Vink et al. (2001), in which case, we used the latter. For the eWNE phase – when $0.05 > X_{\rm s}$ and the ratio of the mass fractions of $(^{12}{\rm C}+{}^{16}{\rm O})/^{4}{\rm He} < 0.03$ – and WC/WO phases – when $(^{12}{\rm C}+{}^{16}{\rm O})/^{4}{\rm He} > 0.03$ – we used the corresponding prescriptions of Nugis & Lamers (2000). Note also that both the Nugis & Lamers (2000) and Gräfener & Hamann (2008) mass-loss rates account for clumping effects (Muijres et al. 2011).

As is discussed below, the mass-loss rates from Nugis & Lamers (2000) for the eWNE phase are much larger than in other phases and thus the largest mass loss occurs during this phase. In Crowther et al. (2010), the mass-loss prescription from Nugis & Lamers (2000) was used for both the eWNL and eWNE phases. The current models thus lose less mass than those presented in Crowther et al. (2010) during the eWNL phase.

The metallicity dependence of the mass-loss rates is included in the following way. The mass-loss rate used at a given metallicity, $\dot M(Z)$, is the mass-loss rate at solar metallicity, $\dot M({\rm Z}_\odot)$, multiplied by the ratio of the metallicities to the power of α: $\dot M(Z) = \dot M({\rm Z}_\odot)(Z/{\rm Z}_\odot)^{\alpha}$. α was set to 0.85 for the O-type phase and WN phase and 0.66 for the WC and WO phases; and for WR stars the initial metallicity rather than the actual surface metallicity was used in the equation above following Eldridge & Vink (2006). α was set to 0.5 for the de Jager et al. (1988) prescription. Finally, α was set to 0 (no dependence) if $\log(T_{\rm eff}) \leq 3.7$ (note that none of the models presented in this study reaches such low effective temperatures).

For rotating models, we applied to the radiative mass-loss rate the correction factor described in Maeder & Meynet (2000a):

$$\dot M(\Omega) = F_\Omega \dot M(\Omega = 0)$$

$$\text{with}\quad F_\Omega = \frac{(1-\Gamma)^{\frac{1}{\alpha}-1}}{\left[1-\frac{\Omega^2}{2\pi G\rho_{\rm m}}-\Gamma\right]^{\frac{1}{\alpha}-1}}, \qquad (1)$$

where $\Gamma = L/L_{\rm Edd} = \kappa L/(4\pi c G M)$ is the Eddington factor (with κ the total opacity), and α the $T_{\rm eff}$-dependent force multiplier parameter.

Table 2. Main properties at the start of the core H-burning phase (ZAMS). $M_{\rm ini}$ is the initial mass, $Z_{\rm ini}$ is the initial metallicity, $\upsilon_{\rm eq}$ is the equatorial velocity in km s^{-1}, $L_{\rm ZAMS}$ is the luminosity, $T_{\rm eff}^{\rm ZAMS}$ is the effective luminosity and $\Gamma_{\rm Edd}^{\rm ZAMS}$ is the Eddington limit.

$M_{\rm ini}$	$Z_{\rm ini}$	$\upsilon_{\rm eq}$	$L_{\rm ZAMS}$	$T_{\rm eff}^{\rm ZAMS}$	$\Gamma_{\rm Edd}^{\rm ZAMS}$
120	0.014	0	6.231	4.729	0.376
150	0.014	0	6.383	4.736	0.426
200	0.014	0	6.567	4.739	0.489
300	0.014	0	6.812	4.734	0.572
500	0.014	0	7.099	4.705	0.666
120	0.014	373	6.230	4.727	0.374
150	0.014	395	6.373	4.723	0.417
200	0.014	411	6.558	4.723	0.479
300	0.014	426	6.804	4.716	0.564
500	0.014	361	7.098	4.694	0.717
120	0.006	0	6.227	4.750	0.376
150	0.006	0	6.379	4.758	0.426
500	0.006	0	7.091	4.754	0.660
120	0.006	400	6.214	4.737	0.365
150	0.006	404	6.377	4.756	0.425
200	0.006	440	6.552	4.751	0.477
300	0.006	468	6.798	4.753	0.560
500	0.006	415	7.091	4.754	0.666
150	0.002	436	6.377	4.778	0.426
200	0.002	443	6.550	4.776	0.477
300	0.002	509	6.793	4.780	0.557

2.2 Models computed

We calculated models of 120, 150, 200, 300 and 500 M$_\odot$. The initial properties of the models are listed in Table 2. The zero-age main sequence (ZAMS) is chosen as the time when 0.3 per cent in mass fraction of hydrogen is burnt. Although we focused our study on rotating stellar models, we also calculated non-rotating models at solar and LMC metallicities. The initial surface equatorial velocity was chosen in order to have the same ratio of the initial to critical velocity, $\upsilon_{\rm ini}/\upsilon_{\rm crit}$, of 0.4 on the ZAMS for all models in line with Ekström et al. (2012). The surface velocity corresponding to this ratio increases with initial mass, except for the 500 M$_\odot$, for which the very high luminosity reduces the critical velocity (see Maeder & Meynet 2000b, for more details). This choice of initial velocities corresponds to an average velocity on the MS of 97 km s^{-1} for the 120 M$_\odot$ stellar model and 141 km s^{-1} for 500 M$_\odot$ model.

3 RESULTS OF VMS MODELS

3.1 VMS evolve nearly homogeneously

Probably the main characteristic that makes VMS quite different from their lower mass siblings is the fact that they possess very large convective cores during the MS phase. To illustrate this last point, Fig. 1 shows the convective core mass fraction for non-rotating massive stars at solar metallicity. It is apparent that the convective cores for masses above 150 M$_\odot$ extend over more than 75 per cent of the total mass of the star.

Fig. 2 shows how age, metallicity and rotation influence this mass fraction. Comparing the top-left and bottom-left panels showing the rotating 150 M$_\odot$ models at solar and SMC metallicities (Z), respectively, we can see that the convective core occupies a very slightly larger fraction of the total mass at SMC metallicity on the ZAMS. As for lower mass massive stars, this is due to a lower

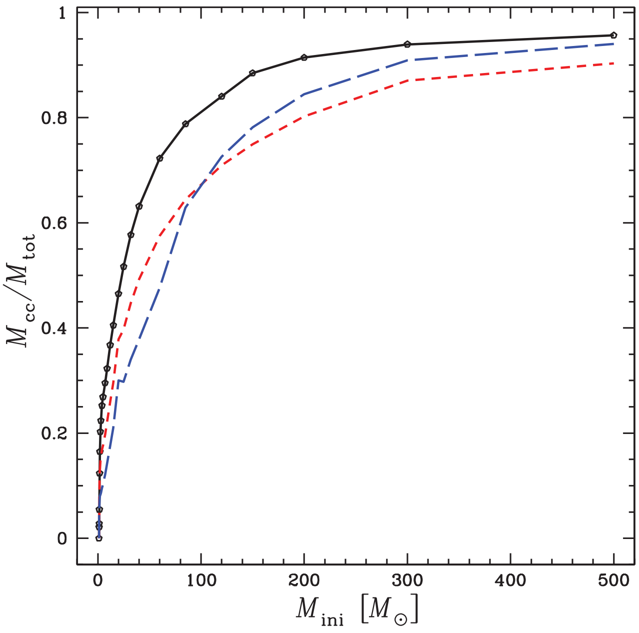

Figure 1. Mass fraction of the convective core in non-rotating solar metallicity models. The models with initial masses superior or equal to 150 $M_\odot$ are from the present work. Models for lower initial masses are from Ekström et al. (2012). The continuous line corresponds to the ZAMS, the short-dashed line to models when the mass fraction of hydrogen at the centre, X_c, is 0.35 and the long-dashed line to models when X_c is equal to 0.05.

CNO content leading to higher central temperature. This effect is counterbalanced by the lower opacity (especially at very low metallicities) and the net change in convective core size is small. As the evolution proceeds mass loss is weaker at lower Z and thus the total mass decreases slower than the convective core mass. This generally leads to a smaller fraction of the total mass occupied by the convective core in the SMC models.

We can see the impact of rotation by comparing the rotating (top-left) and non-rotating (top-right) 150 $M_\odot$ models. The convective core size remains higher in the rotating model due to the additional mixing in radiative zones. We can see that rotation induced mixing can even lead to an increase of the convective core size as is the case for the SMC model (bottom-left). This increase is typical of quasi-homogeneous evolution also found in previous studies (see Yoon, Dierks & Langer 2012, and citations therein). The rotating 500 $M_\odot$ model (bottom right-hand panel) evolves quasi-homogeneously throughout its entire evolution, even with an initial ratio of the velocity to the critical velocity of 0.4.

This feature of the most massive stars is a key factor governing their evolution as is discussed below.

3.2 Evolutionary tracks and lifetimes

In Figs 3–5, we present the evolutionary tracks of our present models with initial masses between 150 and 500 $M_\odot$ for the three metallicities considered. Other properties of the present stellar models are given at various evolutionary stages in Tables 3–5.

A very first striking feature is that these massive stars evolve vertically in the HR diagram (HRD) covering only very restricted ranges in effective temperatures but a very large range in luminosities. This is typical of an evolution mainly governed by mass loss and also by a strong internal mixing (here due to convection).

Let us now describe in more details the evolution of the non-rotating 500 $M_\odot$ model at solar metallicity (see Fig. 3). In general, the luminosity of stars increases during the MS phase. Here we have that during that phase, the luminosity decreases slightly by about 0.1 dex. This is the consequence of very high mass-loss rates (of the order of 7×10^{-5} $M_\odot$ yr^{-1}) already at very early evolutionary stages.

At an age of 1.43 Myr, the mass fraction of hydrogen at the surface becomes inferior to 0.3, the star enters into the WR phase and has an actual mass decreased by about 40 per cent with respect to its initial value. At that time the mass fraction of hydrogen in the core is 0.24. Thus this star enters the WR phase while still burning its hydrogen in its core and having nearly the same amount of hydrogen at the centre and at the surface, illustrating the nearly homogeneous nature of its evolution. Typically for this model, the convective core encompasses nearly 96 per cent of the total mass on the ZAMS (see also Fig. 1).

At an age equal to 2.00 Myr, the mass fraction of hydrogen is zero in the core ($X_c = 0$). The star has lost a huge amount of mass through stellar winds and has at this stage an actual mass of 55.7 $M_\odot$. So, since the entrance into the WR phase, the star has lost about 245 $M_\odot$, i.e. about half of its total mass. This strong mass-loss episode translates into the HRD by a very important decrease in luminosity. Note that when X_c is zero, the convective core still encompass 80 per cent of the total stellar mass!

The core helium burning phase last for about 0.3 Myr, that means slightly more than 15 per cent of the MS lifetime. At the end of the core He-burning phase, the actual mass of the star is 29.82 $M_\odot$, its age is 2.32 Myr, the mass fraction of helium at the surface is 0.26. The last model has an age of 2.32 Myr, an actual mass of 29.75 and a helium surface abundance in mass fraction of 0.06. The total WR phase lasts for 0.88 Myr, that means about 38 per cent of the total stellar lifetime.

It is interesting to compare the evolution of the 500 $M_\odot$ stellar model with that of the 150 $M_\odot$ model. In contrast to the 500 $M_\odot$ model, the 150 $M_\odot$ increases in luminosity during the MS phase. Looking at the HRD we see that the O-type star phases of the 150 and 500 $M_\odot$ models cover more or less the same effective temperature range. This illustrates the well known fact that the colours of stars for this mass range do not change much with the initial mass.

When the stars enters into the WR phase, in contrast to the case of the 500 $M_\odot$ where the luminosity decreases steeply, the luminosity of the 150 $M_\odot$ model continues to increase a little. The luminosities of the two models when the hydrogen mass fraction at the surface becomes inferior to 10^{-5} differ by just a little more than 0.1 dex. The effective temperatures are similar. Thus one expects stars from very different initial masses to occupy similar positions in the HRD (the 500 $M_\odot$ star being slightly less luminous than the 150 $M_\odot$ during the WR phase). We note that after the end of the core He-burning phase, the star evolves to the red and terminate its lifetime around an effective temperature of $\log T_{\mathrm{eff}}$ equal to 4. This comes from the core contraction at the end of core He burning which releases energy and leads to an envelope expansion akin to the expansion of the envelope at the end of the MS (see also Yoshida & Umeda 2011).

The duration of the core H-burning phase of the 150 $M_\odot$ model is not much different from the one of the 500 $M_\odot$ model being 2.5 Myr instead of 2 Myr. The core He-burning lifetime lasts for 0.3 Myr as for the 500 $M_\odot$. The total duration of the WR phase is 0.45 Myr, thus about half of the WR duration for the 500 $M_\odot$.

The 200 $M_\odot$ model has an evolution similar to the 150 $M_\odot$ model, while the 300 $M_\odot$ has an evolution similar to the 500 $M_\odot$.

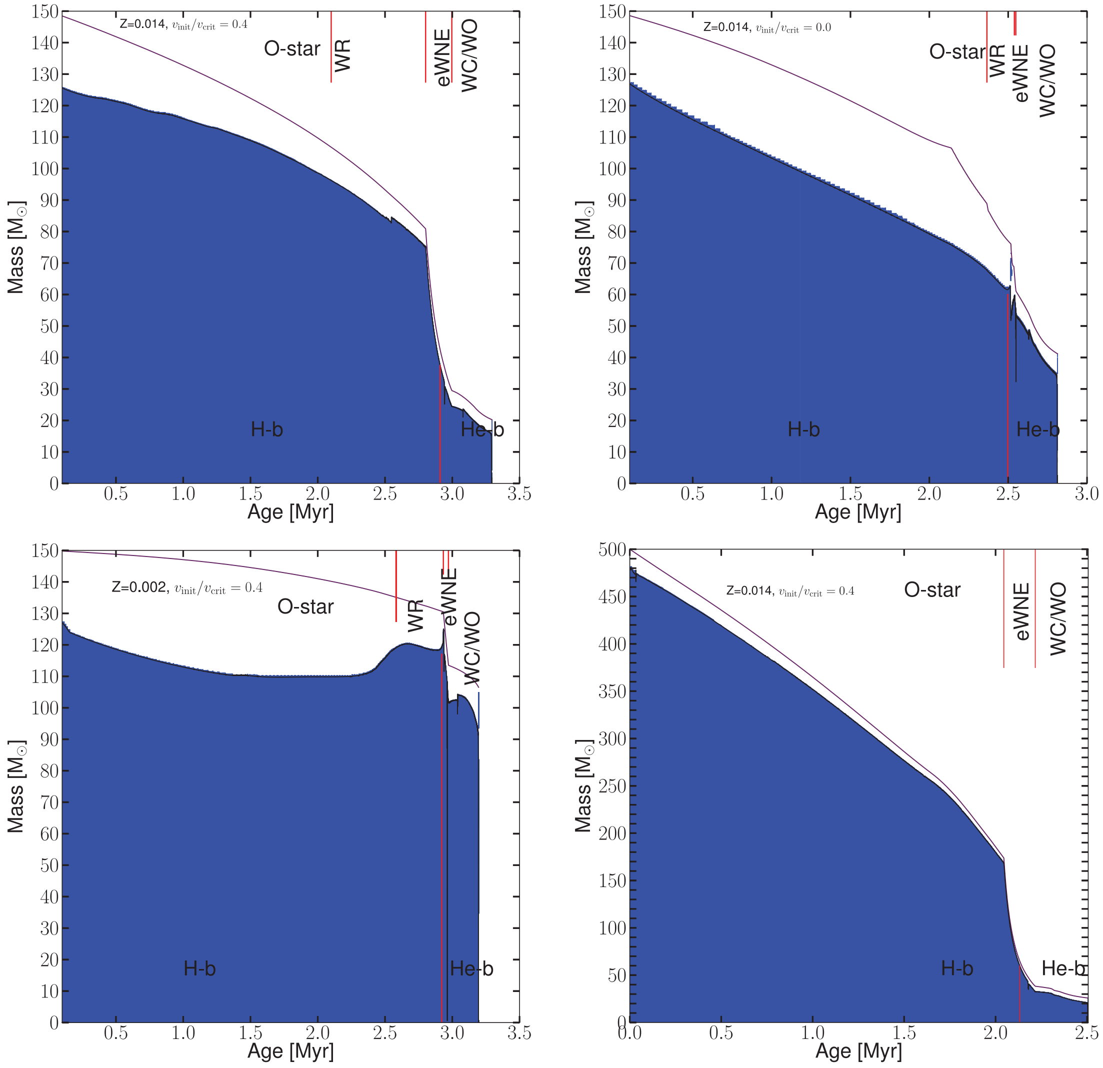

Figure 2. Structure evolution as a function of age for selected models: solar metallicity 150 M$_\odot$ rotating (top-left) and non-rotating (top-right) models, rotating SMC metallicity 150 M$_\odot$ model (bottom-left) and rotating solar metallicity 500 M$_\odot$ model (bottom-right). The blue zones represent the convective regions. The top solid black line indicates the total mass of the star and vertical red markers are given for the different phases (O-type, WR = eWNL, eWNE and WC/WO) at the top of the plots. The transition between H- and He-burning phases is indicated by the red vertical line at the bottom of the plots.

Let us now consider how rotation changes the picture. Fig. 3, right-hand panel, shows the evolutionary tracks of the $Z = 0.014$ rotating tracks in a similar way as in the left-hand panel. The changes brought by rotation are modest. This is expected because of two facts: first, in this high mass range, the evolution is more impacted by mass loss than by rotation, secondly, stars are already well mixed by the large convective cores. One notes however a few differences between the non-rotating and rotating models. One of the most striking is the fact that the models during their O-type phase evolve nearly vertically when rotation is accounted for. This is the effect of rotational mixing which keep the star more homogeneous than in the non-rotating cases (although, as underlined above, already in models with no rotation, due to the importance of the convective core, stars are never very far from chemical homogeneity). As was the case in the non-rotating tracks, the O-type star phase corresponds to an upward displacement when time goes on in the HRD for the 150 M$_\odot$ model, while, it corresponds to a downwards displacement for the three more massive models. One notes finally that lower luminosities are reached by the rotating models at the end of their evolution (decrease by about 0.3 dex in luminosity, thus by a factor of 2). This comes mainly because the rotating models enter earlier into their WR phase and thus lose more mass.

How does a change in metallicity alter the picture? When the metallicity decreases to $Z = 0.006$ (see Fig. 4), as expected, tracks are shifted to higher luminosities and effective temperatures. In this metallicity range, all models evolve upwards during their O-type star phase in the HRD. This is an effect of the lower mass-loss rates.

As was already the case at $Z = 0.014$, rotation makes the star to evolve nearly vertically in the HRD. One notes in this metallicity range, much more important effects of rotation than at $Z = 0.014$, which is also expected, since at these lower metallicity, mass-loss rates are smaller and rotational mixing more efficient. We note that most of the decrease in luminosity in the 500 M$_\odot$ solar mass model occurs during the WC phase in the $Z = 0.006$ non-rotating model, while it occurs during the WNL phase in the rotating one. This illustrates the fact that rotational mixing, by creating a much larger H-rich region in the star, tends to considerably increase the duration of the WNL phase. One notes also that while the 150 M$_\odot$ model enters the WR phase only after the MS phase, the rotating model becomes a WR star before the end of the MS phase.

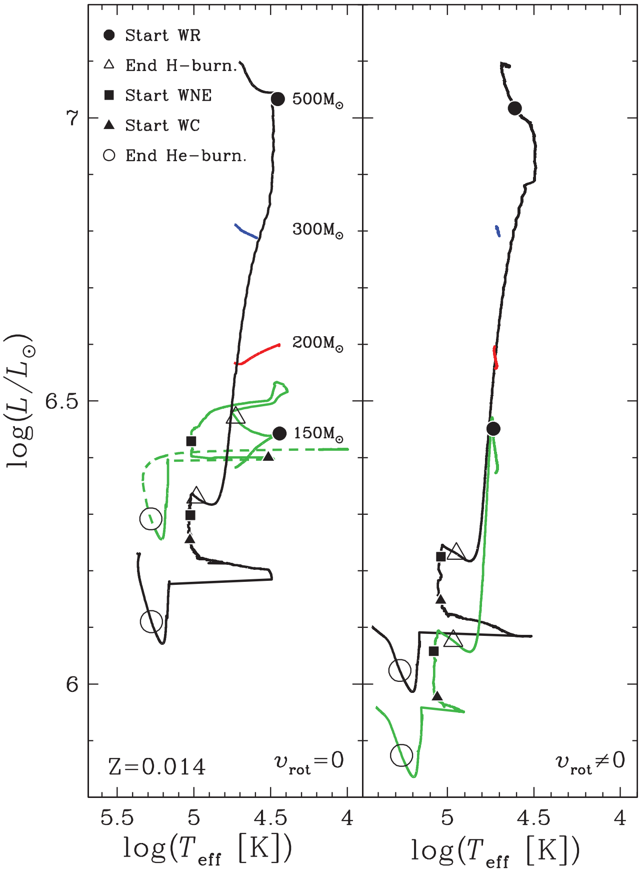

Figure 3. HRD from 150 up to 500 $M_\odot$ at solar metallicity for non-rotating (left) and rotating (right) models, respectively. Key stages are indicated along the tracks. Only the first portion (up to start of WR phase) of the tracks for the 200 and 300 $M_\odot$ is shown.

At the metallicity of the SMC (see Fig. 5), except for the 500 $M_\odot$, the tracks evolve horizontally after the end of the core H-burning phase (triangle in Fig. 5). The much lower mass-loss rates are responsible for this effect.

3.3 Lifetimes and mass–luminosity relation

In Tables 3–5, we provide lifetimes at the end of core hydrogen burning, core helium burning and the total stellar lifetimes, respectively. The end of a burning stage is chosen when the mass fraction of the main fuel becomes less than 10^{-5}. We see that the MS lifetime of non-rotating models at solar metallicity ranges from 2.67 to 1.99 Myr for initial masses ranging from 120 to 500 $M_\odot$ showing the well-known fact that VMS have a very weak lifetime dependence on their initial mass.

The mass–luminosity relation on the ZAMS for rotating massive stars at solar composition is shown in Fig. 6. The relation ($L \propto M^\alpha$) is steep for low- and intermediate-mass stars ($\alpha \sim 3$ for $10 < M/M_\odot < 20$) and flattens for VMS ($\alpha \sim 1.3$ for $200 < M/M_\odot < 500$). This flattening is due to the increased radiation pressure relative to gas pressure in massive stars. Since the lifetime of a star is roughly M/L, we get that for VMS $\tau \propto M/L \propto M^{-0.3}$.

The H-burning (and total) lifetimes of VMS are lengthened by rotation as in lower mass stars. Differences in the H-burning lifetimes

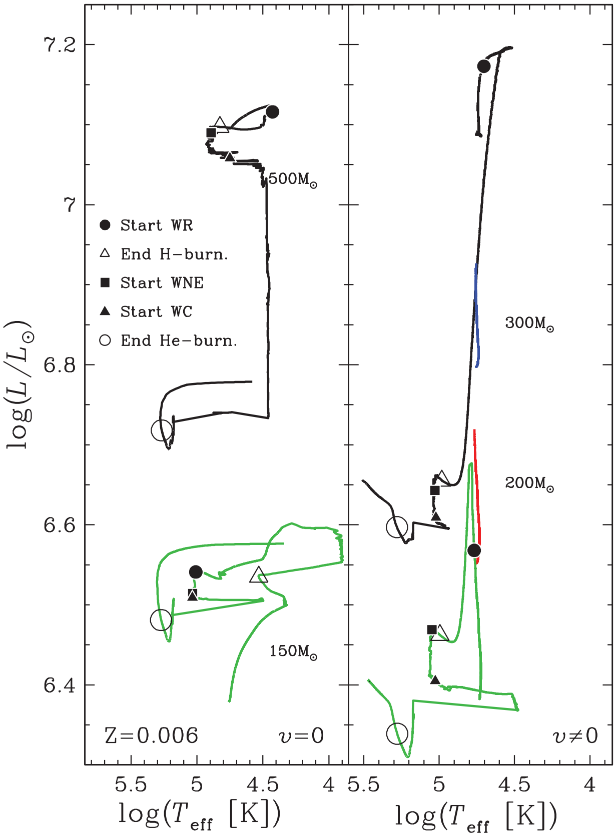

Figure 4. Same as Fig. 3 for LMC models ($Z = 0.006$).

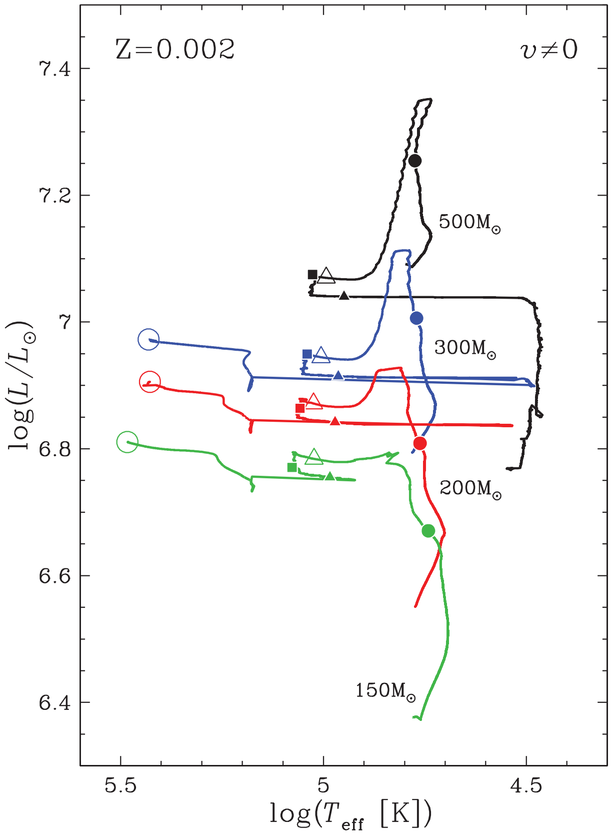

Figure 5. Same as Fig. 3 (right) for SMC rotating models ($Z = 0.002$).

Table 3. Properties of the hydrogen-burning phase: initial properties of stellar models (columns 1–3), lifetime of H-burning and O-type star phase (columns 4 and 5), average MS surface velocity (column 6) and properties at the end of the core H-burning phase (columns 7–15). Masses are in solar masses, velocities are in km s^{-1}, lifetimes are in 10^6 yr and abundances are surface abundances in mass fractions. The luminosity, L, is in $\log_{10}(L/{\rm L}_\odot)$ unit and the effective temperature, $T_{\rm eff}$, is in $\log_{10}$ (K). Note that the effective temperature given here includes a correction for WR stars to take into account the fact that their winds are optically thick as in Meynet & Maeder (2005).

$M_{\rm ini}$	$Z_{\rm ini}$	$\frac{v_{\rm ini}}{v_{\rm crit}}$	$\tau_{\rm H}$	$\tau_{\rm o}$	$\langle v_{\rm MS}\rangle$	$M^{\rm end}_{\rm H.b.}$	^{1}H	^{4}He	^{12}C	^{14}N	^{16}O	$T_{\rm eff}$	L	$\Gamma_{\rm Edd}$
120	0.014	0.0	2.671	2.592	0.0	63.7	2.04e-1	7.82e-1	8.58e-5	8.15e-3	1.06e-4	4.405	6.334	0.627
150	0.014	0.0	2.497	2.348	0.0	76.3	1.35e-1	8.51e-1	9.26e-5	8.15e-3	9.91e-5	4.413	6.455	0.657
200	0.014	0.0	2.323	2.095	0.0	95.2	7.51e-2	9.11e-1	9.93e-5	8.14e-3	9.23e-5	4.405	6.597	0.687
300	0.014	0.0	2.154	1.657	0.0	65.2	1.24e-3	9.85e-1	1.31e-4	8.11e-3	7.93e-5	4.267	6.401	0.595
500	0.014	0.0	1.990	1.421	0.0	56.3	2.20e-3	9.84e-1	1.26e-4	8.12e-3	8.03e-5	4.301	6.318	0.568
120	0.014	0.4	3.137	2.270	116.71	34.6	1.56e-3	9.85e-1	1.33e-4	8.10e-3	8.48e-5	4.400	6.018	0.463
150	0.014	0.4	2.909	2.074	101.24	37.1	1.80e-3	9.85e-1	1.30e-4	8.11e-3	8.41e-5	4.387	6.062	0.479
200	0.014	0.4	2.649	1.830	89.33	40.0	1.41e-3	9.85e-1	1.33e-4	8.10e-3	8.30e-5	4.372	6.110	0.495
300	0.014	0.4	2.376	1.561	61.16	43.2	1.85e-3	9.85e-1	1.33e-4	8.10e-3	8.23e-5	4.356	6.157	0.511
500	0.014	0.4	2.132	1.377	24.55	48.1	1.24e-3	9.85e-1	1.38e-4	8.10e-3	8.08e-5	4.332	6.221	0.531
120	0.006	0.0	2.675	2.682	0.0	79.0	4.03e-1	5.91e-1	3.29e-5	3.50e-3	4.47e-5	4.441	6.391	0.672
150	0.006	0.0	2.492	2.499	0.0	96.1	3.28e-1	6.67e-1	3.58e-5	3.50e-3	4.25e-5	4.483	6.524	0.709
500	0.006	0.0	1.904	1.636	0.0	238.8	2.56e-2	9.69e-1	5.12e-5	3.48e-3	3.18e-5	4.032	7.094	0.819
120	0.006	0.4	3.140	2.479	208.55	64.0	1.70e-3	9.92e-1	6.06e-5	3.47e-3	3.04e-5	4.387	6.395	0.597
150	0.006	0.4	2.857	2.172	198.19	71.3	9.76e-4	9.93e-1	6.33e-5	3.47e-3	2.97e-5	4.365	6.455	0.615
200	0.006	0.4	2.590	1.894	193.05	80.7	1.22e-3	9.93e-1	6.29e-5	3.47e-3	2.95e-5	4.339	6.525	0.638
300	0.006	0.4	2.318	1.619	173.47	85.8	1.32e-3	9.93e-1	6.30e-5	3.47e-3	2.93e-5	4.327	6.559	0.649
500	0.006	0.4	2.077	1.419	116.76	101.7	1.37e-3	9.93e-1	6.37e-5	3.47e-3	2.89e-5	4.291	6.650	0.676
150	0.002	0.4	2.921	2.567	318.92	128.8	1.67e-3	9.96e-1	2.13e-5	1.16e-3	8.09e-6	4.394	6.780	0.720
200	0.002	0.4	2.612	2.168	333.43	152.2	1.31e-3	9.97e-1	2.26e-5	1.16e-3	7.82e-6	4.363	6.867	0.743
300	0.002	0.4	2.315	1.801	347.32	176.2	1.10e-3	9.97e-1	2.32e-5	1.16e-3	7.68e-6	4.279	7.067	0.763

Table 4. Properties of the helium-burning phase: initial properties of stellar models (columns 1–3), age of star at the end of He burning (column 4), average He-b. surface velocity (column 5) and properties at the end of the core He-burning phase (columns 6–15). Abundances are given for the surface, except for ^{12}C$_{\rm c}$, which represents the central C abundance. Same units as in Table 3. $\mathcal{L}_{\rm CO}$ [$10^{50}\,\frac{\rm g\,cm^2}{\rm s}$] is the angular momentum contained in the CO core (note that at this stage the angular velocity is constant in the CO core due to convective mixing).

$M_{\rm ini}$	$Z_{\rm ini}$	$\frac{v_{\rm ini}}{v_{\rm crit}}$	${\rm Age}^{\rm end}_{\rm He\text{-}b.}$	$\langle v_{\rm He\text{-}b.}\rangle$	$M^{\rm end}_{\rm He\text{-}b.}$	^{4}He	^{12}C	^{12}C$_{\rm c}$	^{16}O	^{22}Ne	$T_{\rm eff}$	L	$\Gamma_{\rm Edd}$	$\mathcal{L}_{\rm CO}$
120	0.014	0.0	3.003	0.00	30.9	0.242	0.458	0.150	0.281	1.081e-02	4.819	6.117	0.650	0
150	0.014	0.0	2.809	0.00	41.3	0.234	0.436	0.126	0.312	1.003e-02	4.822	6.278	0.706	0
200	0.014	0.0	2.622	0.00	49.4	0.207	0.408	0.112	0.366	8.811e-03	4.807	6.377	0.737	0
300	0.014	0.0	2.469	0.00	38.2	0.234	0.443	0.133	0.305	1.029e-02	4.825	6.236	0.691	0
500	0.014	0.0	2.314	0.00	29.8	0.261	0.464	0.152	0.257	1.110e-02	4.811	6.095	0.640	0
120	0.014	0.4	3.513	1.58	18.8	0.292	0.492	0.195	0.198	1.196e-02	4.806	5.814	0.533	1.91
150	0.014	0.4	3.291	1.18	20.3	0.286	0.488	0.187	0.208	1.184e-02	4.808	5.863	0.551	1.91
200	0.014	0.4	3.020	0.50	22.0	0.277	0.484	0.180	0.221	1.172e-02	4.812	5.912	0.570	1.37
300	0.014	0.4	2.733	0.13	24.0	0.270	0.479	0.172	0.233	1.151e-02	4.814	5.965	0.589	0.75
500	0.014	0.4	2.502	0.03	25.9	0.269	0.473	0.164	0.239	1.140e-02	4.811	6.010	0.606	0.28
120	0.006	0.0	2.993	0.00	54.2	0.229	0.391	0.098	0.372	3.701e-03	4.860	6.424	0.753	0
150	0.006	0.0	2.845	0.00	59.7	0.241	0.370	0.086	0.380	3.597e-03	4.844	6.474	0.767	0
500	0.006	0.0	2.182	0.00	94.7	0.251	0.392	0.078	0.349	3.318e-03	4.833	6.711	0.834	0
120	0.006	0.4	3.472	6.84	39.3	0.294	0.457	0.132	0.241	4.709e-03	4.387	6.395	0.692	16.2
150	0.006	0.4	3.164	3.67	45.7	0.310	0.451	0.122	0.231	4.701e-03	4.824	6.329	0.767	14.7
200	0.006	0.4	2.904	1.33	51.1	0.303	0.444	0.114	0.245	4.547e-03	4.825	6.390	0.738	9.98
300	0.006	0.4	2.625	0.35	54.1	0.291	0.439	0.110	0.262	4.433e-03	4.830	6.421	0.748	5.18
500	0.006	0.4	2.387	0.13	74.9	0.330	0.425	0.090	0.237	4.356e-03	4.790	6.590	0.798	4.83
150	0.002	0.4	3.193	64.94	106.7	0.809	0.153	0.074	0.035	1.730e-03	4.743	6.766	0.841	412.5
200	0.002	0.4	2.889	29.88	129.3	0.880	0.109	0.066	0.009	1.777e-03	4.789	6.861	0.863	355.6
300	0.002	0.4	2.585	5.10	149.8	0.938	0.058	0.060	0.001	1.798e-03	4.833	6.933	0.880	156.8

Table 5. Key properties at the end of the calculations (last model): initial properties of stellar models (columns 1–3), burning stage corresponding to the last model (column 4), total lifetime (column 5), average surface velocity after core He burning (column 6) and properties at the last model (columns 7–14). Same units as in Table 3.

$M_{\rm ini}$	$Z_{\rm ini}$	$\frac{v_{\rm ini}}{v_{\rm crit}}$	Last model	Lifetime	$\langle v_{\rm s}\rangle$	$M_{\rm f}$	^{4}He	^{12}C	^{16}O	^{22}Ne	$T_{\rm eff}$	L	$\Gamma_{\rm Edd}$
120	0.014	0.0	End O-b.	3.007	0.00	30.8	2.376e-01	4.568e-01	2.872e-01	1.075e-02	4.791	6.252	0.892
150	0.014	0.0	End C-b.	2.813	0.00	41.2	2.268e-01	4.332e-01	3.214e-01	9.910e-03	4.009	6.414	0.969
200	0.014	0.0	End C-b.	2.625	0.00	49.3	1.949e-01	4.014e-01	3.848e-01	8.505e-03	4.000	6.486	0.955
300	0.014	0.0	End O-b.	2.473	0.00	38.2	2.309e-01	4.418e-01	3.088e-01	1.025e-02	4.479	6.380	0.966
500	0.014	0.0	End O-b.	2.318	0.00	29.8	2.562e-01	4.629e-01	2.626e-01	1.106e-02	4.844	6.229	0.875
120	0.014	0.4	End O-b.	3.517	15.18	18.7	2.858e-01	4.925e-01	2.035e-01	1.193e-02	4.865	5.907	0.664
150	0.014	0.4	End O-b.	3.295	0.78	20.2	2.797e-01	4.884e-01	2.138e-01	1.181e-02	4.867	5.954	0.692
200	0.014	0.4	End Ne-b.	3.025	1.88	21.9	2.712e-01	4.838e-01	2.267e-01	1.168e-02	4.878	6.008	0.714
300	0.014	0.4	End O-b.	2.737	22.81	23.9	2.650e-01	4.784e-01	2.384e-01	1.148e-02	4.879	6.056	0.731
500	0.014	0.4	End Ne-b.	2.507	0.03	25.8	2.643e-01	4.726e-01	2.449e-01	1.136e-02	4.879	6.101	0.751
120	0.006	0.0	End He-b.	2.996	0.00	54.2	2.286e-01	3.911e-01	3.722e-01	3.701e-03	4.860	6.424	0.753
150	0.006	0.0	End He-b.	2.848	0.00	59.7	2.413e-01	3.702e-01	3.804e-01	3.597e-03	4.844	6.474	0.768
500	0.006	0.0	End He-b.	2.185	0.00	94.7	2.509e-01	3.919e-01	3.490e-01	3.318e-03	4.833	6.711	0.834
120	0.006	0.4	End O-b.	3.476	27.47	39.2	2.889e-01	4.567e-01	2.465e-01	4.687e-03	4.896	6.327	0.832
150	0.006	0.4	End Ne-b.	3.167	8.39	45.6	3.057e-01	4.505e-01	2.360e-01	4.680e-03	4.897	6.403	0.852
200	0.006	0.4	End O-b.	2.907	25.36	51.0	2.982e-01	4.436e-01	2.503e-01	4.524e-03	4.898	6.460	0.869
300	0.006	0.4	End O-b.	2.629	0.17	54.0	2.856e-01	4.383e-01	2.681e-01	4.400e-03	4.907	6.490	0.879
500	0.006	0.4	End O-b.	2.390	0.28	74.8	3.220e-01	4.249e-01	2.452e-01	4.307e-03	4.871	6.655	0.929
150	0.002	0.4	End O-b.	3.196	160.57	106.5	7.922e-01	1.634e-01	4.177e-02	1.717e-03	4.828	6.810	0.932
200	0.002	0.4	End O-b.	2.889	187.90	129.2	8.730e-01	1.131e-01	1.137e-02	1.773e-03	4.867	6.905	0.956
300	0.002	0.4	End O-b.	2.587	10.72	149.7	9.362e-01	5.969e-02	1.487e-03	1.797e-03	4.934	6.970	0.959

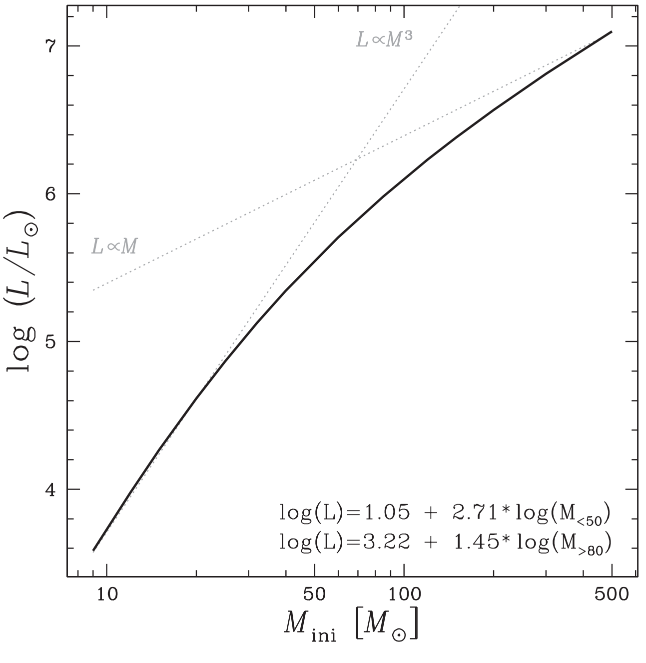

Figure 6. Mass–luminosity relation on the ZAMS for rotating models at solar metallicity. The formulae in the bottom right-hand corner are linear fits for the mass ranges 9–50 and 80–500 $M_\odot$. As can be seen in Table 2, the non-rotating models have very similar properties on the ZAMS.

of rotating and non-rotating 150 $M_\odot$ models at solar metallicity are ∼14 per cent. The effects of metallicity on the lifetimes are generally very small. The small differences in total lifetimes are due to different mass loss at different metallicities.

3.4 Mass loss by stellar winds

Mass loss by stellar winds is a key factor governing the evolution of VMS. This comes from the very high luminosities reached by these objects. For example, the luminosity derived for R136a1 is about 10 million times that of our Sun.

For such luminous objects, winds will be very powerful at all evolutionary stages, so while early MS VMS are formally O-type stars from an evolutionary perspective, their spectral appearance may be closer to Of or Of/WN at early phases (Crowther, Hirschi & Walborn 2012).

Table 6 gives the total mass at the start and end of the evolution as well as at the transitions between the different WR phases in columns 1–5. The average mass-loss rates during the O-type and eWNE phases (the phase during which the mass-loss rates are highest) are given in columns 6 and 7, respectively.

The evolution of the mass-loss rates for various models is shown in Fig. 7. Following the evolution from left to right for the 150 $M_\odot$ model at solar metallicity (solid black), mass-loss rates slowly increase at the start of the O-type phase with mass-loss rates between 10^{-5} (absolute values for the mass-loss rates, $-\dot{M}$, are quoted in this paragraph) and $10^{-4.5}$. If a bi-stability limit is encountered during the O-type phase, as is the case in the non-rotating 150 $M_\odot$ model, mass-loss rates can vary significantly over a short period of time and mass loss peaks reach values higher than 10^{-4}. The highest mass-loss rate is encountered at the start of the eWNE phase (star symbols) with values in excess of 10^{-3} (note that the mass-loss rate in the non-rotating model has a peak at the end of the H-burning phase, phase due to the star reaching temporarily cooler effective temperatures). Such high mass-loss rates quickly reduce the mass and luminosity of the star and thus the mass-loss rate also decreases quickly during the eWNE phase. During the WC/WO phase, mass-loss

Table 6. Mass-loss properties: total mass of the models at various stages (columns 1–5), and average mass-loss rates $\langle \dot{M} \rangle$ during the O-type and eWNE phases (columns 6 and 7). Masses are in solar mass units and mass-loss rates are given in $M_\odot$ yr^{-1}.

ZAMS	End O-type/start eWNL	End eWNL/start eWNE	End eWNE/start WC	Final	$\langle \dot{M}_{\rm Vink} \rangle$	$\langle \dot{M}_{\rm eWNE} \rangle$
	$Z = 0.014$, $\upsilon/\upsilon_{\rm crit} = 0.0$					
120	69.43	52.59	47.62	30.81	2.477e-05	3.638e-04
150	88.86	66.87	61.20	41.16	3.274e-05	6.107e-04
200	121.06	91.20	83.85	49.32	4.618e-05	1.150e-03
300	184.27	130.47	52.05	38.15	8.047e-05	8.912e-04
500	298.79	169.50	45.14	29.75	1.736e-04	9.590e-04
	$Z = 0.014$, $\upsilon/\upsilon_{\rm crit} = 0.4$					
120	88.28	69.54	27.43	18.68	1.675e-05	2.057e-04
150	106.64	80.88	29.49	20.22	2.467e-05	2.640e-04
200	137.52	98.75	31.84	21.93	3.985e-05	3.564e-04
300	196.64	129.10	34.45	23.93	7.559e-05	5.160e-04
500	298.42	174.05	38.30	25.83	1.594e-04	7.901e-04
	$Z = 0.006$, $\upsilon/\upsilon_{\rm crit} = 0.0$					
120	74.30	57.91	56.91	54.11	2.140e-05	3.272e-04
150	94.18	74.20	71.75	59.59	2.839e-05	5.038e-04
500	332.68	250.64	197.41	94.56	1.304e-04	3.334e-03
	$Z = 0.006$, $\upsilon/\upsilon_{\rm crit} = 0.4$					
120	100.57	90.78	54.43	39.25	9.429e-06	3.219e-04
150	125.79	111.84	60.75	45.58	1.367e-05	4.418e-04
200	166.81	144.86	66.25	51.02	2.180e-05	6.257e-04
300	247.07	207.10	73.11	54.04	4.166e-05	9.524e-04
500	397.34	315.51	86.10	74.75	9.194e-05	1.685e-03
	$Z = 0.002$, $\upsilon/\upsilon_{\rm crit} = 0.4$					
150	135.06	130.46	113.51	106.50	6.661e-06	4.485e-04
200	181.42	174.18	137.90	129.21	9.902e-06	6.631e-04
300	273.18	260.81	156.14	149.70	1.730e-05	1.040e-03

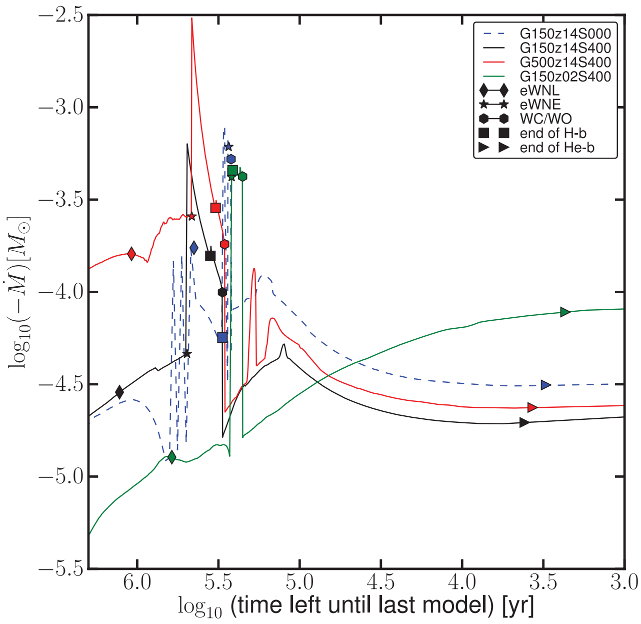

Figure 7. Evolution of the mass-loss rate as a function of time left until last model (log scale) for the rotating 500 $M_\odot$ model (solid-red), the rotating 150 $M_\odot$ model (solid-black), the non-rotating (dashed) 150 $M_\odot$ model at solar metallicity and the rotating 150 $M_\odot$ model at SMC metallicity (solid-green). The diamonds indicate the start of the eWNL phase, the stars the start of the eWNE phase and hexagons the start of the WC/WO phase. The squares and triangles indicate the end of H-b. and He-b. phases, respectively.

rates are of the same order of magnitude as during the O-type phase.

Comparing the rotating 500 and 150 $M_\odot$ model at solar metallicity (solid black and red), we see that more massive stars start with higher mass-loss rates but converge later on to similar mass-loss rates since the total mass of the models converges to similar values (see Table 6).

Comparing the SMC and solar metallicity 150 $M_\odot$ rotating models, we can clearly see the metallicity effect during the O-type star phase. During the eWNE phase, mass-loss rates are similar and in the WC/WO, mass-loss rates in the SMC model are actually higher since the total mass in that model remained high in contrast with solar metallicity models.

Table 6 also shows the relative importance of the mass lost during the various phases and how their importance changes as a function of metallicity. Even though mass loss is the strongest during the eWNE phase, significant amount of mass is lost in all phases.

3.5 Mass-loss rates and proximity of the Eddington limit

Recently, Gräfener et al. (2011) suggested enhanced mass-loss rates (with respect to Vink et al. 2001) for stars with high Eddington parameters ($\Gamma_{\rm Edd} \geq 0.7$) that they attribute to the WR stage. In the present work, we did not use such a mass-loss rate prescription. In order to know whether it would have had an impact on the present result, we discuss here the proximity of our models to the Eddington limit.

Fig. 8 shows the Eddington parameter, $\Gamma_{\rm Edd} = L/L_{\rm Edd} = \kappa L/(4\pi c G M)$, as a function of the initial mass of our models at

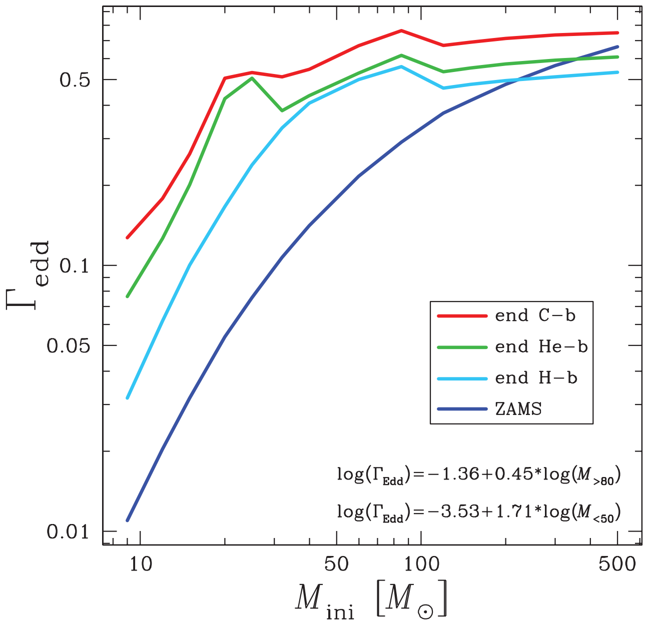

Figure 8. Eddington parameter, Γ_{edd}, for rotating models at solar metallicity. Γ_{edd} is plotted on the ZAMS (blue line) and the end of H-(light blue), He-(green) and C-burning (red) phases. Except for the 300 and 500 $\mathrm{M}_\odot$ models, Γ_{edd} increases throughout the evolution. At solar metallicity, the highest value (close to 0.8) is actually reached by the 85 $\mathrm{M}_\odot$ model at the end of its evolution. This could lead to significant mass loss shortly before the final explosion in a model that ends as a WR star and potentially explain supernova surrounded by a thick circumstellar material without the need for the star to be in the luminous variable phase. The formulae in the bottom right-hand corner are linear fits for the mass ranges: 9–50 and 80–500 $\mathrm{M}_\odot$. As can be seen in Table 2, the non-rotating models have very similar properties on the ZAMS.

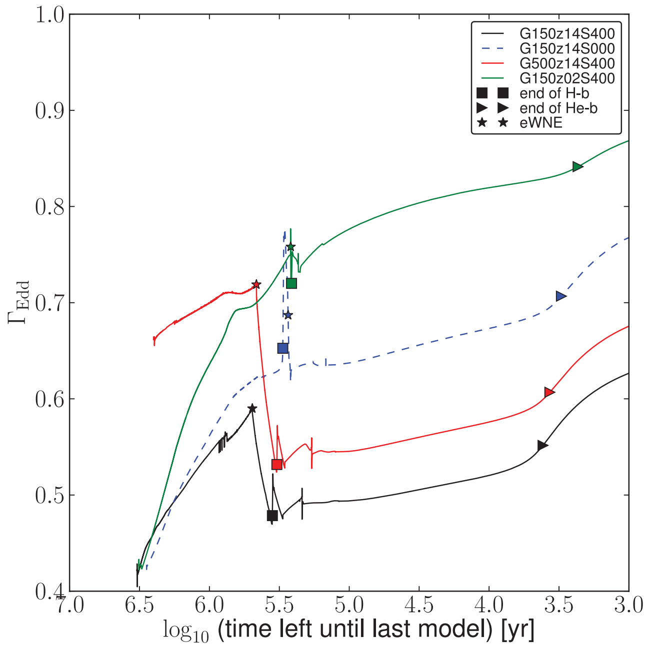

Figure 9. Evolution of the Eddington parameter, Γ_{Edd}, as a function of time left until last model (log scale) for the rotating 500 $\mathrm{M}_\odot$ model (solid red), the rotating 150 $\mathrm{M}_\odot$ model (solid black), the non-rotating (dashed) 150 $\mathrm{M}_\odot$ model at solar metallicity and the rotating 150 $\mathrm{M}_\odot$ model at SMC metallicity (solid green). The stars indicate the start of the eWNE phase. The squares and triangles indicate the end of H-b. and He-b. phases, respectively.

key stages (see also Table 2). Since the Eddington parameter, Γ_{Edd} scales with L/M, the curve for Γ_{Edd} also flattens for VMS. The ZAMS values for Γ_{Edd} range between 0.4 and 0.6, so well below the Eddington limit, $\Gamma_{\mathrm{Edd}} = 1$, and below the limiting value of 0.7 where enhanced mass-loss rates are expected according to Gräfener et al. (2011).

How does Γ_{Edd} change during the lifetime of VMS? Fig. 9 presents the evolution of Γ_{Edd} for a subset of representative models. The numerical values for each model are given at key stages in Tables 3–5. Since $\Gamma_{\mathrm{Edd}} \propto \kappa L/M$, an increase in luminosity and a decrease in mass both lead to higher Γ_{Edd}. Changes in effective temperature and chemical composition affect the opacity and also lead to changes in Γ_{Edd}.

In rotating models at solar metallicity, Γ_{Edd} slowly increases until the start of the eWNE phase. This is mainly due to the increase in luminosity and decrease in mass of the model. At the start of the eWNE phase, mass loss increases significantly. This leads to a strong decrease in the luminosity of the model and as a result Γ_{Edd} decreases sharply.

During the WC/WO phase, mass-loss rates being of similar values as during the O-type star phase, Γ_{Edd} increases again gradually.

We can see that, at solar metallicity, Γ_{Edd} rarely increases beyond 0.7 even in the 500 $\mathrm{M}_\odot$ model. There are nevertheless two interesting cases in which values above 0.7 are reached. The first case is during the advanced stages. At this stage, mass loss does not have much time to change the total mass of the star (it is mostly changes in effective temperature and to a minor extent in luminosity that influence the increase in Γ_{Edd}). This may nevertheless trigger instabilities resulting in strong mass-loss episodes. This may have consequences for the type of SN event that such star will produce and may be a reason why the explosion of VMS may look like as if they had happened in environment similar to those observed around Luminous Blue Variable. The second case is at low metallicity, as highlighted by the 150 $\mathrm{M}_\odot$ model. Indeed, values above 0.7 are reached before the end of the MS (square symbol). We plan to determine the impact of using mass-loss prescriptions such as the ones of Gräfener et al. (2011) and Maeder et al. (2012) on the fate of VMS in a forthcoming study. The non-rotating model has a different mass-loss history (see Fig. 7), which explains the slightly different evolution of Γ_{Edd} near the end of the MS.

3.6 Evolution of the surface velocity

The surface velocity of stars is affected by several processes. Contraction or expansion of the surface, respectively, increases and decreases the surface velocity due to conservation of angular momentum. Mass loss removes angular momentum and thus decreases the surface velocity. Finally, internal transport of angular momentum generally increases the surface velocity. As shown in Fig. 10 (left-hand panel), at solar metallicity, the surface velocity rapidly decreases during the MS due to the strong mass loss over the entire mass range of VMS. At SMC metallicity, mass loss is weaker and internal transport of angular momentum initially dominate over mass loss and the surface velocity increases during the first half of the MS phase. During this time, the ratio of surface velocity to critical velocity also increases up to values close to 0.7 (note that our models include the effect of the luminosity of the star when determining the critical rotation as described in Maeder & Meynet 2000a). However, at SMC metallicity, in contrast with very low

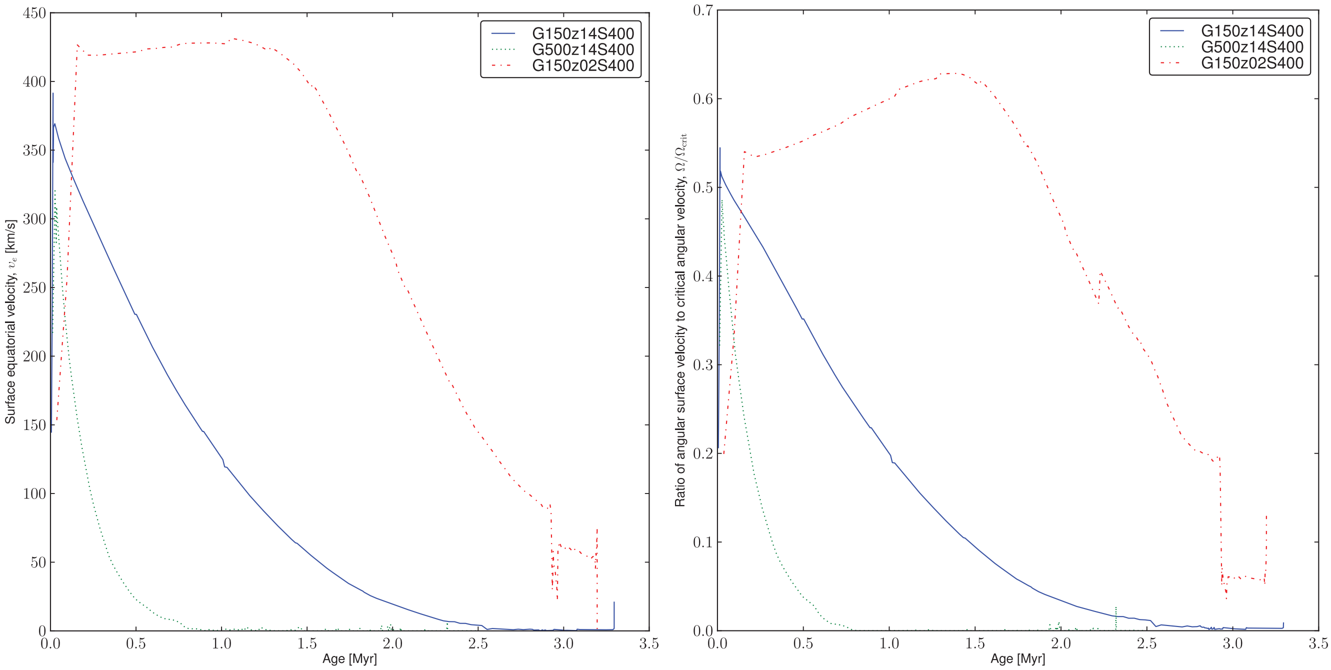

Figure 10. Evolution of surface equatorial velocity (left) and ratio of the surface angular velocity to the critical angular velocity (right) for the rotating solar metallicity 150 and 500 $M_\odot$ and SMC 150 $M_\odot$ models as a function of age of the star.

and zero metallicity stars (Hirschi 2007; Ekström et al. 2008; Chatzopoulos & Wheeler 2012; Yoon et al. 2012), mass loss eventually starts to dominate and the surface velocity and its ratio to critical rotation both decrease for the rest of the evolution. SMC stars thus never reach critical rotation. The angular momentum content in the core of VMS stars is discussed in Section 5.3.

4 WR STARS FROM VMS

In Fig. 11, we present the evolution of the surface abundances as a function of the total mass for the solar metallicity rotating models of 150 and 60 $M_\odot$. This figure shows how the combined effects of mass loss and internal mixing change their surface composition. Qualitatively there are no big differences between the 60 and 150 $M_\odot$ models. Since the 150 $M_\odot$ has larger cores, the transition to the various WR stages occurs at larger total masses compared to the 60 $M_\odot$ model. It thus confirms the general idea that a more massive (thus more luminous) WR star originates from a more massive O-type star. Fig. 11 shows that all abundances and abundance ratios are very similar for a given WR phase. it is therefore not possible to distinguish a WR originating from a VMS from its surface chemical composition (however see below).

We present in Table 7 the lifetimes of the different WR phases through which all our VMS models evolve. At solar metallicity, the WR phase of non-rotating stellar models for masses between 150 and 500 $M_\odot$ covers between 16 and 38 per cent of the total stellar lifetime. This is a significantly larger proportion than for masses between 20 and 120 $M_\odot$, where the WR phase covers only 0–13 per cent of the total stellar lifetimes. At the LMC metallicity, the proportion of the total stellar lifetime spent as a WR phase for VMS decreases to values between 12 (150 $M_\odot$) and 25 per cent (500 $M_\odot$).

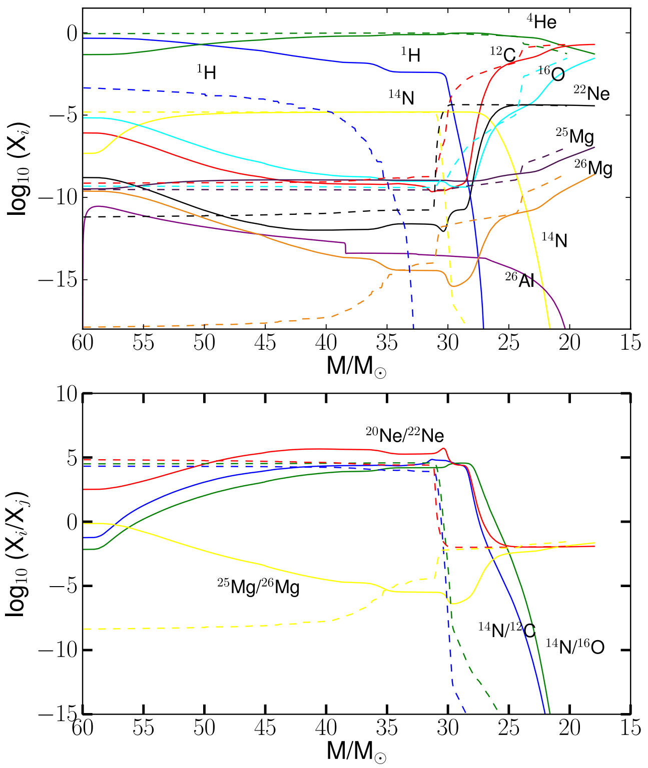

Figure 11. Evolution of surface abundances of the solar metallicity rotating 150 $M_\odot$ (solid) and 60 $M_\odot$ (dashed) rotating solar *Z* models as a function of total mass (evolution goes from left to right since mass loss peels off the star and reduces the total mass). The top panel shows individual abundances while the bottom panel shows abundance ratios.

Table 7. Lifetimes of the various phases in units of years.

$M_{\rm ini}$	$Z_{\rm ini}$	$\frac{v_{\rm ini}}{v_{\rm crit}}$	O-star	WR	WNL	WNE	WN/WC	WC (WO)
120	0.014	0	2.151e-06	3.959e-05	1.150e-05	9.390e-03	2.675e-02	2.715e-05
150	0.014	0	2.041e-06	4.473e-05	1.777e-05	5.654e-03	7.120e-02	2.639e-05
200	0.014	0	1.968e-06	5.148e-05	2.503e-05	1.773e-03	4.576e-02	2.626e-05
300	0.014	0	1.671e-06	8.014e-05	5.051e-05	9.217e-03	2.735e-03	2.870e-05
500	0.014	0	1.286e-06	8.848e-05	5.804e-05	1.079e-04	3.279e-03	2.935e-05
120	0.014	0.4	2.289e-06	1.227e-06	8.790e-05	4.118e-04	4.008e-03	3.076e-05
150	0.014	0.4	2.105e-06	1.189e-06	8.567e-05	2.579e-04	3.649e-03	3.068e-05
200	0.014	0.4	1.860e-06	1.164e-06	8.375e-05	2.242e-04	3.153e-03	3.042e-05
300	0.014	0.4	1.585e-06	1.152e-06	8.315e-05	1.897e-04	2.897e-03	3.015e-05
500	0.014	0.4	1.422e-06	1.083e-06	7.663e-05	1.830e-04	2.899e-03	2.990e-05
120	0.006	0	2.222e-06	2.964e-05	2.043e-05	1.302e-02	6.025e-02	9.202e-04
150	0.006	0	2.028e-06	3.320e-05	1.579e-05	1.211e-03	2.921e-02	1.728e-05
500	0.006	0	1.388e-06	5.362e-05	2.690e-05	5.211e-03	1.350e-03	2.620e-05
120	0.006	0.4	2.513e-06	9.624e-05	6.776e-05	1.601e-04	3.386e-03	2.687e-05
150	0.006	0.4	2.188e-06	9.789e-05	6.912e-05	2.172e-04	2.336e-03	2.660e-05
200	0.006	0.4	1.922e-06	9.848e-05	7.073e-05	1.347e-04	2.757e-03	2.640e-05
300	0.006	0.4	1.644e-06	9.838e-05	7.033e-05	1.600e-04	9.744e-02	2.644e-05
500	0.006	0.4	1.461e-06	9.283e-05	6.647e-05	9.312e-03	6.853e-02	2.542e-05
150	0.002	0.4	2.583e-06	6.119e-05	3.691e-05	8.459e-03	4.874e-03	2.343e-05
200	0.002	0.4	2.196e-06	6.926e-05	4.524e-05	1.019e-04	2.709e-03	2.300e-05
300	0.002	0.4	1.827e-06	7.602e-05	5.186e-05	1.317e-04	1.289e-03	2.283e-05

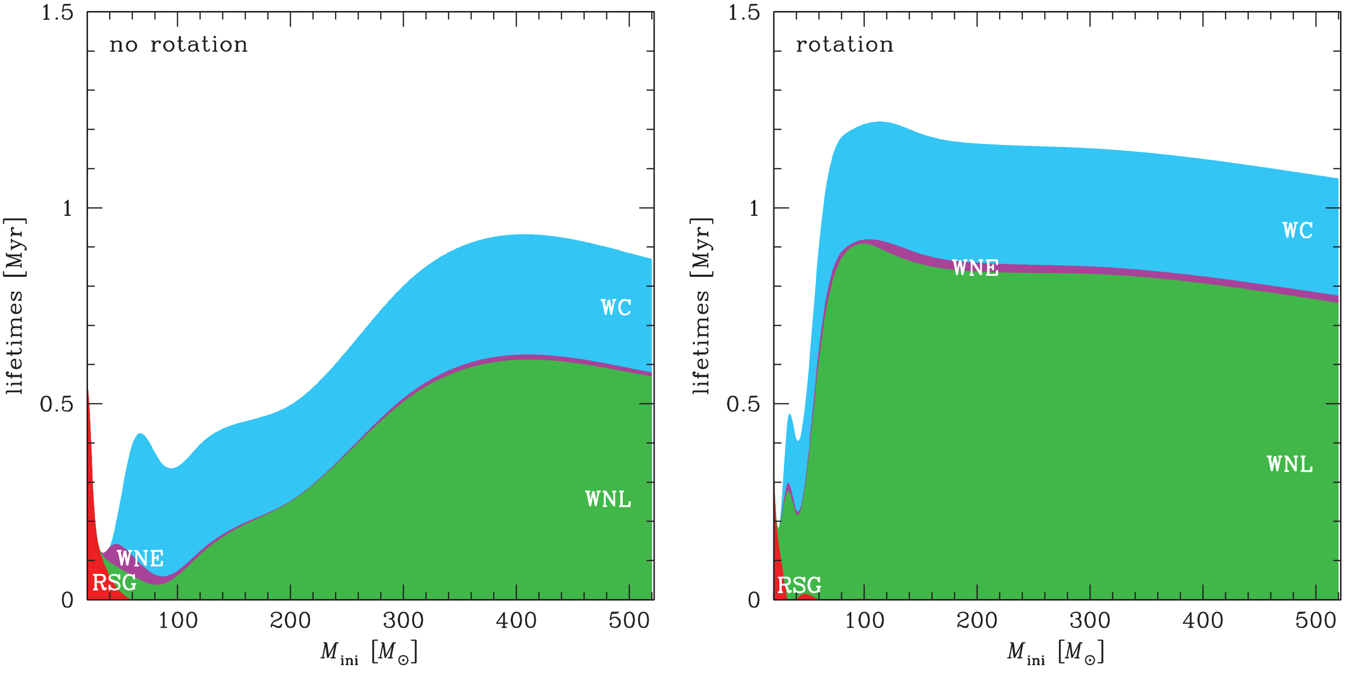

Figure 12. Lifetimes of the red supergiant (RSG phase and of the different WR phases for the solar metallicity non-rotating (left) and rotating (right) models. Lifetimes are piled up. For example, the lifetime of the WNE phase extent corresponds to the height of the purple area.

Fig. 12 shows how these lifetimes varies as a function of mass for our non-rotating and rotating solar metallicity models. Looking first at the non-rotating models (Fig. 12, left), we see that the VMS (above 150 $M_\odot$) have WR lifetimes between 0.4 and nearly 1 Myr. The longest WR phase is the WNL phase since these stars spend a large fraction of H burning in this phase. The duration of the WC phases of VMS is not so much different from those of stars in the mass range between 50 and 120 $M_\odot$.

Rotation significantly increases the WR lifetimes. Typically, the WR phase of rotating stellar models for masses between 150 and 500 $M_\odot$ covers between 36 and 43 per cent of the total stellar lifetime. The increase is more important for the lower mass range plotted in the figures. This reflects the fact that for lower initial mass stars, mass-loss rates are weaker and thus the mixing induced by rotation has a greater impact. We see that this increase is mostly due to longer durations for the WNL phase, the WC phase duration remaining more or less constant for the whole mass range between 50 and 500 $M_\odot$ as was the case for the non-rotating models. Rotation has qualitatively similar effects at the LMC metallicities.

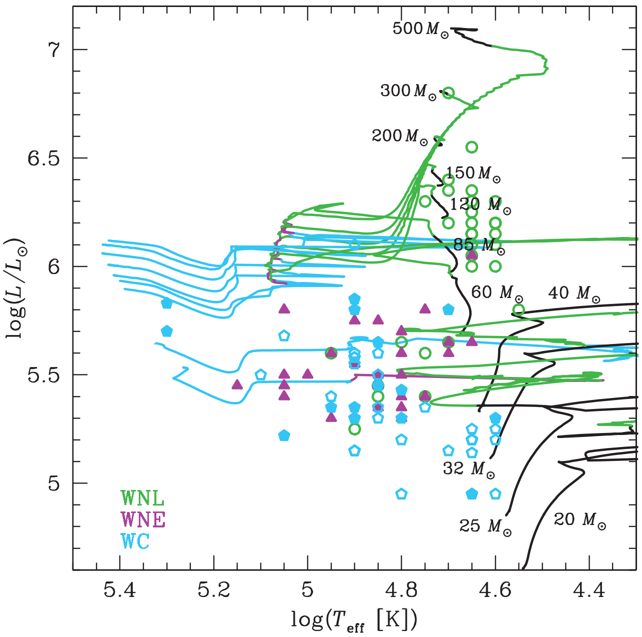

Figure 13. The positions of WR stars observed by Hamann, Gräfener & Liermann (2006) and Sander, Hamann & Todt (2012) are indicated with the rotating evolutionary tracks taken from Ekström et al. (2012) for masses up to 120 $M_\odot$ and from the present work above.

Would the account of the VMS stars in the computation of the number ratios of WR to O-type stars and on the WN/WC ratios have a significant effect? The inclusion of VMS is marginal at solar metallicity, since the durations are only affected by a factor of 2. Convoluted with the weighting of the initial mass function (IMF), WR stars originating from VMS only represent ~10 per cent of the whole population of WR stars (using a Salpeter 1955, IMF) originating from single stars. However, the situation is different at SMC metallicity. Because of the weakness of the stellar winds, single stellar models below 120 $M_\odot$ at this Z do not produce any WC or WO stars (Georgy et al., in preparation). In that case, we expect that the few WC/WO stars observed at low metallicity come from VMS, or from the binary channel (Eldridge, Izzard & Tout 2008). In starburst regions, the detection of WR stars at very young ages would also be an indication that they come from VMS, as these stars enter the WR phase before their less massive counterparts, and well before WRs coming from the binary channel.

We see in Fig. 13 that the present VMS models well fit the most luminous WNL stars. On the other hand, they predict very luminous WC stars. Of course the fact that no such luminous WC stars has ever been observed can simply come from the fact that such stars are very rare and the lifetime in the WC phase is moreover relatively short.

4.1 The final chemical structure

Fig. 14 shows the chemical structure at the last time-steps calculated, which is the end of the carbon-burning phase in the case of the 40 $M_\odot$, and the end of the core oxygen-burning phase in the case of the 150 and 500 $M_\odot$ models. A few interesting points come out from considering this figure. First, in all cases, some helium is still present in the outer layers. Depending on how the final stellar explosion occur, this helium may or may not be apparent in the spectrum, as discussed in Section 5. Secondly, just below the He-burning shell, products of the core He burning, not affected by further carbon burning are apparent. This zone extends between about 4 and 10 $M_\odot$ in the 40 $M_\odot$ model, between about 32 and 35 $M_\odot$ in the 150 $M_\odot$ model and in a tiny region centred around 24 $M_\odot$ in the 500 $M_\odot$ model. We therefore see that this zone decreases in importance when the initial mass increases. Interestingly, the chemical composition in this zone present striking differences if we compare for instance the 40 and the 500 $M_\odot$ model. We can see that the abundance of ^{20}Ne is much higher in the more massive model. This comes from the fact that in more massive stars, due to higher central temperatures during the core He-burning phase the reaction ^{16}O(α, γ)^{20}Ne is more active, building thus more ^{20}Ne. Note that ^{24}Mg is also more abundant, which is natural since the reaction ^{20}Ne(α, γ)^{24}Mg will also be somewhat active in VMS for the same reasons. While in the case of the 150 $M_\odot$, due to the mass-loss history, the ^{20}Ne and ^{24}Mg-rich layers are not uncovered, they are uncovered in the 500 $M_\odot$ model. This implies that strong overabundances of these two isotopes at the surface of WC stars can be taken as a signature for an initially VMS as the progenitor of that WC star. It means also that, contrary to what occurs at the surface of WC stars originating from lower initial mass stars, neon is no longer present mainly in the form of ^{22}Ne (and thus be a measure of the initial CNO content since resulting from the transformation of nitrogen produced by CNO burning during the H-burning phase) but will mainly be present in the form of ^{20}Ne.

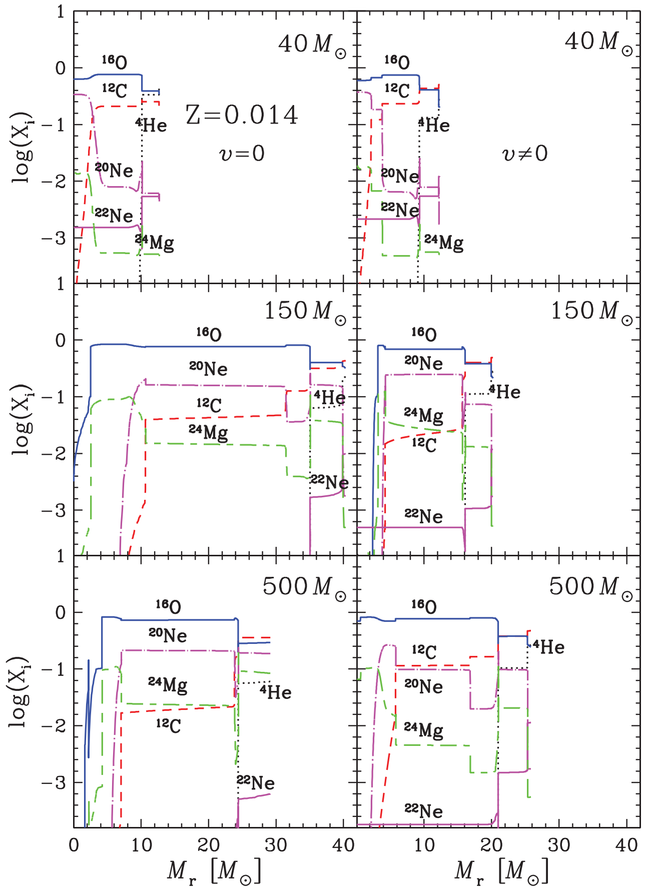

Figure 14. Chemical structure of 40, 150 and 500 $M_\odot$ non-rotating (left) and rotating (right) models at $Z = 0.014$ at the end of the calculations. Note that the rotating 500 $M_\odot$ model is shown at an earlier evolutionary stage than the corresponding non-rotating model.

Rotation does not change much this picture (see right-hand panel of Fig. 14), except that, due to different mass-loss histories, the rotating models lose much more mass and end their evolution with smaller cores. This is particularly striking for the 150 $M_\odot$ model. Qualitatively the situation is not much different at lower metallicities.

5 FATE OF VERY MASSIVE STARS

The best way to predict the fate of our models would be to simulate their evolution and final explosion, which we have done for a subset of the models with the KEPLER code (as described below) but whether or not a star produces a PCSN can be reasonably estimated from the mass of its carbon–oxygen (CO) core as demonstrated by the similar fate for stars with the same CO core found in various studies of VMS in the early Universe (Bond, Arnett & Carr 1984; Heger & Woosley 2002; Chatzopoulos & Wheeler 2012; Dessart et al. 2013), even if their prior evolution is different. Our models also confirm the idea that the CO core mass is a good indicator for the advanced evolution and thus the fate of the models. Indeed, as discussed below, stars with a wide range of initial masses at solar metallicity end with a very similar total mass at the end of He burning (thus a very similar CO core mass) and they have extremely similar evolution during the advanced stages. In this section, we will thus use the CO core mass to estimate the fate of the models. It is important to stress that for lower mass massive stars ($\lesssim 50\,M_\odot$), the CO core mass alone is not sufficient to predict the fate of the star and other factors like compactness, rotation and the central carbon abundance at the end of helium burning also play a role (see e.g. Chieffi & Limongi 2013). We will also discuss the supernova types that these VMS may produce.

5.1 Advanced phases, final masses and masses of carbon–oxygen cores

In Fig. 15, the structure evolution diagrams are drawn as a function of the log of the time left until the last model calculated (as opposed to age used in Fig. 2). This choice of *x*-axis allows one to see the evolution of the structure during the advanced stages. In the left-hand panel, we can see that, at solar metallicity, VMS have an advanced evolution identical to lower mass stars (see e.g. fig. 12 in Hirschi et al. 2004) with a radiative core C burning followed by a large convective C-burning shell, radiative neon burning and convective oxygen and silicon-burning stages. All the solar metallicity models will eventually undergo core collapse after going through the usual advanced burning stages. As presented in Table 4 (column 9), the central mass fraction of ^{12}C is very low in all VMS models and is anticorrelated with the total mass at the end of helium burning (column 6): the higher the total mass, the lower the central ^{12}C mass fraction. This is due to the higher temperature is more massive cores leading to a more efficient $^{12}\mathrm{C}(\alpha,\gamma)^{16}\mathrm{O}$ relative to 3α.

The similarities between VMS and lower mass stars at solar metallicity during the advanced stages can also be seen in the central temperature versus central density diagram (see Fig. 16). Even the evolution of the 500 $M_\odot$ rotating model is close to that of the 60 $M_\odot$ model. The non-rotating models lose less mass as described above and thus their evolutionary track is higher (see e.g. the track for the non-rotating 150 $M_\odot$ model in Fig. 16). Non-rotating models nevertheless stay clear of the pair-instability region ($\Gamma < 4/3$, where Γ is the adiabatic index) in the centre.

The situation is quite different at SMC metallicity (right-hand panel). Mass loss is weaker and thus the CO core is very large (93.5 $M_\odot$ for this 150 $M_\odot$ model). Such a large core starts the advanced stages in a similar way: radiative core C burning followed by a large convective C-burning shell and radiative neon burning. The evolution starts to diverge from this point onwards. As can be seen in T_c versus ρ_c plot, the SMC 150 $M_\odot$ model enters the pair-instability region. These models will thus have a different final fate than those at solar metallicity (see below).

Fig. 17 (see also Table 6) shows the final masses obtained in the present models as a function of the initial masses. All models at solar *Z*, rotating or not, end with a small fraction of their initial mass due to the strong mass losses they experience. Rotation enhances mass loss by allowing the star to enter the WR phase earlier during the MS (see top panels of Fig. 2) and the final mass of non-rotating models is generally higher than that of rotating models. At low metallicities,

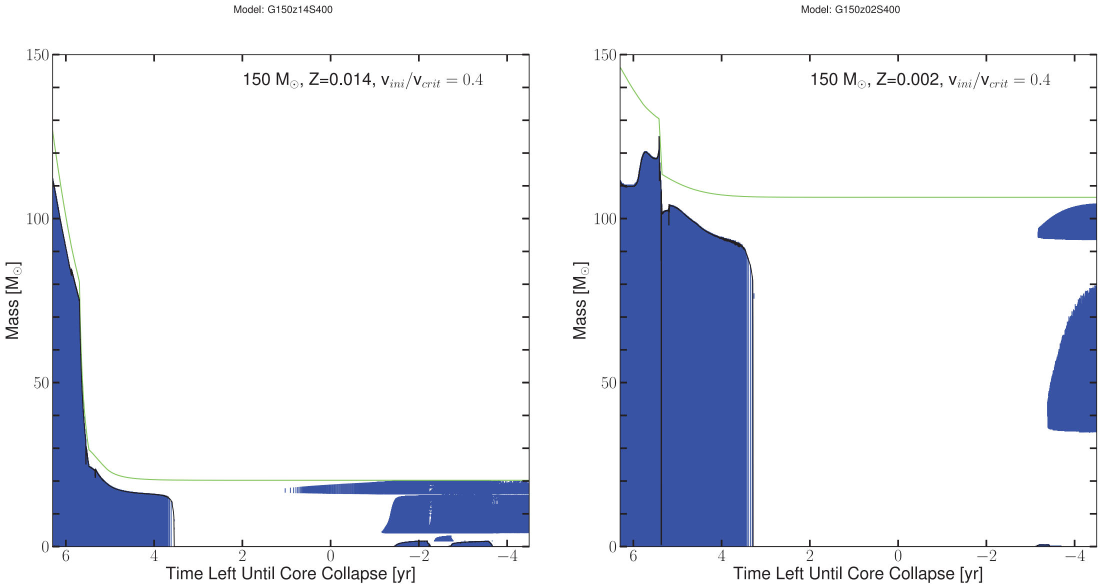

Figure 15. Structure evolution diagram for rotating 150 $M_\odot$ at solar and SMC metallicities as a function of the log of the time left until the last model. The blue zones represent the convective regions.

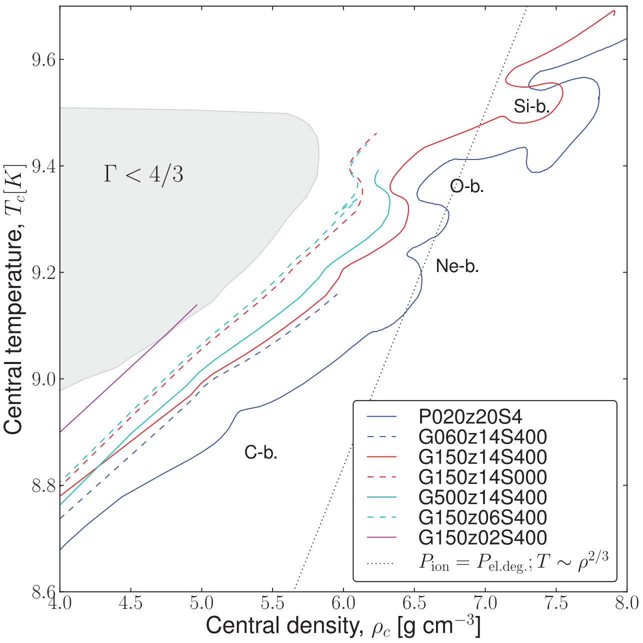

Figure 16. Evolution of the central temperature T_c versus central density ρ_c for the rotating 20 (from Hirschi et al. 2004), 60 (from Ekström et al. 2012), 150 and 500 M$_\odot$ models and non-rotating 150 M$_\odot$ model at solar metallicity as well as the rotating 150 M$_\odot$ model at SMC metallicity. The grey shaded area is the pair-creation instability region ($\Gamma < 4/3$, where Γ is the adiabatic index). The additional dotted line corresponds to the limit between non-degenerate and degenerate electron gas.

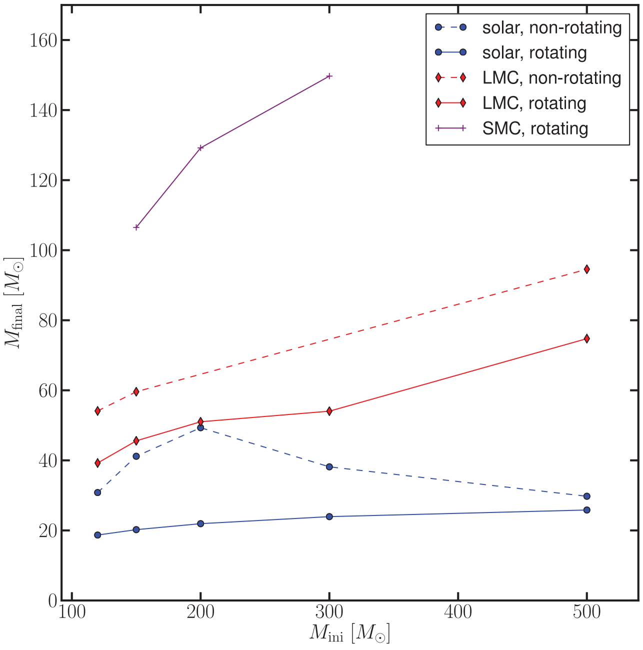

Figure 17. Final mass versus initial mass for all our rotating (solid lines) and non-rotating (dashed line) models.

due to the metallicity dependence of radiatively driven stellar winds in both O-type stars (Vink et al. 2001) and WR stars (Eldridge & Vink 2006), final masses are larger.

Fig. 18 shows how the CO core masses vary as a function of the initial mass, rotation and metallicity. The CO core ($M_{\rm CO}$) is here defined as the core mass for which the mass fraction of C+O is greater than 75 per cent. Since the CO core mass is so close to the total mass, the behaviour is the same as for the total mass and for the same reasons. For the rotating solar metallicity models, mass loss is so strong that all models end with roughly the same CO core mass around 20 M$_\odot$. As the metallicity decreases, so does mass loss and thus the LMC and SMC models have higher final CO core masses and the CO core mass does depend on the initial mass in a monotonous way. Finally, non-rotating models lose less mass than their rotating counterpart since they enter the WR phase later and also have less hot surface.

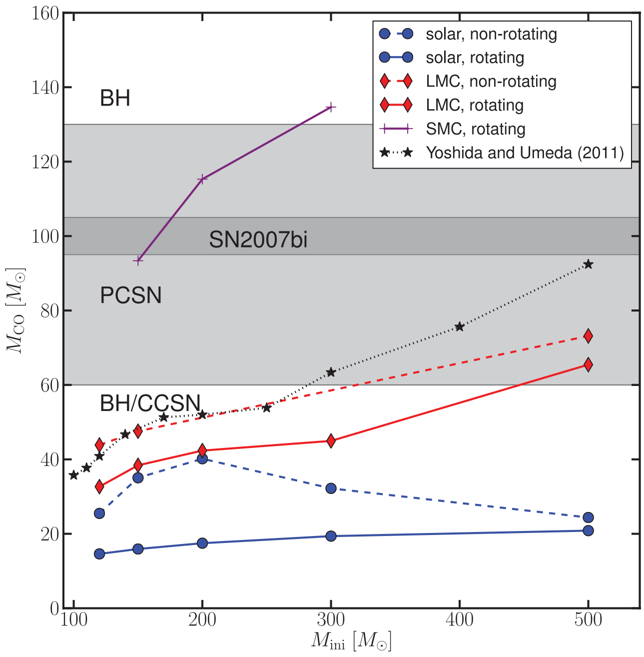

Figure 18. Mass of carbon–oxygen core of all the models as a function of the initial mass. The light grey shaded area represents the range of $M_{\rm CO}$, for which the estimated fate is a PCSN. The thin dark grey shaded area corresponds to the estimated $M_{\rm CO}$ of the progenitor of SN 2007bi assuming it is a PCSN (see text for more details). The points linked by the dotted black line are from the models of Yoshida & Umeda (2011) at $Z = 0.004$, case A.

We see in Fig. 18 that the final CO core mass of our non-rotating models at $Z = 0.006$ is slightly smaller than those obtained for non-rotating stars at $Z = 0.004$ by Yoshida & Umeda (2011). We have also compared the evolutionary tracks in the HRD of our non-rotating LMC models and the models of Yoshida & Umeda (2011) case A and found them to be qualitatively very similar.

As discussed above, the core masses, especially the CO core masses, can be used to estimate whether or not our models produce PCSN by using the results of previous studies, which follow the explosion of such massive cores and knowing that VMS with the same CO core masses have similar core evolution from carbon burning onwards. Heger & Woosley (2002) calculated a grid of models and found that stars with helium cores (M_α) between 64 and 133 M$_\odot$ produce PCSN and that stars with more massive M_α will collapse to a black hole (BH) without explosion, confirming the results of previous studies, such as Bond et al. (1984). The independent results of Chatzopoulos & Wheeler (2012) also confirm the CO core mass range that produces PCSNe.

Let us recall here that PCSNe occur when VMS experience an instability in their core during the neon/oxygen burning stage due to the creation of electron–positron pairs out of two photons. The creation of pairs in their oxygen-rich core softens the equation of

Table 8. Initial masses, mass content of helium in the envelope, mass of carbon–oxygen core, final mass in solar masses and fate of the models.

	Non-rotating				Rotating			
$M_{\rm ini}$	$M_{\rm He}^{\rm env}$	$M_{\rm co}$	$M_{\rm final}$	Fate	$M_{\rm He}^{\rm env}$	$M_{\rm co}$	$M_{\rm final}$	Fate
				$Z = 0.014$				
120	0.4874	25.478	30.8	CCSN/BH	0.5147	18.414	18.7	CCSN/BH
150	0.6142	35.047	41.2	CCSN/BH	0.5053	19.942	20.2	CCSN/BH
200	0.7765	42.781	49.3	CCSN/BH	0.5101	21.601	21.9	CCSN/BH
300	0.3467	32.204	38.2	CCSN/BH	0.4974	19.468	23.9	CCSN/BH
500	0.3119	24.380	29.8	CCSN/BH	0.5675	20.993	25.8	CCSN/BH
				$Z = 0.006$				
120	1.2289	43.851	54.2	CCSN/BH	0.5665	32.669	39.2	CCSN/BH
150	1.1041	47.562	59.7	CCSN/BH	0.7845	38.436	45.6	CCSN/BH
200	–	–	–	CCSN/BH	0.5055	42.357	51.0	CCSN/BH
300	–	–	–	CCSN/BH	0.5802	44.959	54.0	CCSN/BH
500	1.6428	92.547	94.7	PCSN	0.7865	73.145	74.8	PCSN
				$Z = 0.002$				
150	–	–	–	–	2.3353	93.468	106.5	PCSN
200	–	–	–	–	3.3022	124.329	129.2	PCSN
300	–	–	–	–	5.5018	134.869	149.7	BH

state, leading to further contraction. This runaway collapse is predicted to produce a very powerful explosion, in excess of 10^{53} erg, disrupting the entire star and leaving no remnant (Bond et al. 1984; Fryer, Woosley & Heger 2001).

Heger & Woosley (2002) also find that stars with M_α between roughly 40 and 63 $M_\odot$ will undergo violent pulsations induced by the pair instability leading to strong mass loss but which will not be sufficient to disrupt the core. Thus these stars will eventually undergo core collapse as lower mass stars. Since in our models, the CO core masses are very close to M_α (equal to the final total mass in our models, see Table 8), in this study we assume that our models will produce a PCSN if $60 \le M_{\rm CO} \le 130$ $M_\odot$. In Fig. 18, the light grey shaded region corresponds to the zone where one would expect a PCSN, the dark shaded region shows the estimated range of the carbon–oxygen core of the progenitor of SN 2007bi, as discussed below.

We see in Fig. 18 that at solar metallicity none of our models is expected to explode as a PCSN. At the metallicity of the LMC, only stars with initial masses above 450 for the rotating models and above about 300 $M_\odot$ for the non-rotating case are expected to explode as a PCSN. At the SMC metallicity, the mass range for the PCSN progenitors is much more favourable. Extrapolating the points obtained from our models we obtain that all stars in the mass range between about 100 and 290 $M_\odot$ could produce PCSNe. Thus our models provide support for the occurrence of PCSNe in the nearby (not so metal poor) universe.

As mentioned earlier, the evolution of a subset of models (the SMC rotating 150, 200 and 300 $M_\odot$ models and the LMC rotating and non-rotating 500 $M_\odot$ models) has been followed from the end of core helium burning through to explosions with the KEPLER code. The KEPLER simulations confirm that the SMC rotating 150 and 200 $M_\odot$ models and the rotating and non-rotating 500 $M_\odot$ LMC models indeed end as a PCSN and their properties will be presented in a forthcoming paper (Whalen et al., in preparation).

Table 8 presents for each of the models, the initial mass ($M_{\rm ini}$), the amount of helium left in the star at the end of the calculation ($M_{\rm He}^{\rm env}$) and final total mass as well as the predicted fate in terms of the explosion type: PCSN or core-collapse supernova and BH formation with or without mass ejection (CCSN/BH). The helium core mass (M_α) is not given since it is always equal to the final total mass, all our models having lost the entire hydrogen-rich layers.

5.2 Supernova types produced by VMS and comparison to observed superluminous SNe

Let us recall that, in VMS, convective cores are very large. It is larger than 90 per cent above 200 $M_\odot$ at the start of the evolution and even though it decreases slightly during the evolution, at the end of core H burning, the convective core occupies more than half of the initial mass in non-rotating models and most of the star in rotating models. This has an important implication concerning the type of supernovae that these VMS will produce. Indeed, even if mass loss is not very strong in SMC models, all the models we have calculated have lost the entire hydrogen-rich layers long before the end of helium burning. Thus our models predict that all VMS stars in the metallicity range studied will produce either a Type Ib SN (SNIb) or Type Ic SN (SNIc) but no Type II SN (SNII). Since SN 2006gy is a SNIIn (Smith et al. 2007), our models support the idea that the SNIIn is due to interaction with circumstellar material rather than by a PCSN from a VMS that had retained its H-rich envelope as discussed in Smith et al. (2007).

Our models clearly predict no SNeII but it is not so clear whether the VMS that we modelled will produce SNeIb or SNeIc The distinctive feature of SNeIc is the absence of He I lines in their spectra. The absence of lines, however, is not necessarily indicative of a complete absence of helium (see e.g. Dessart et al. 2012a). Other factors such as temperature, density in the region where helium is present are important for the strength of lines. Thus from a theoretical point of view, we are left with some freedom to chose the criterion deciding on whether a star will produce a SNIb or SNIc.

A first approach is based on the total He mass in the envelope. Wellstein & Langer (1999) and Yoon, Woosley & Langer (2010) choose 0.5 $M_\odot$ while Georgy et al. (2009) proposed 0.6 $M_\odot$ as their limit. However, Georgy et al. (2009) also reported that the choice of He mass limit between 0.6 and 1.5 $M_\odot$ hardly affects the mass of MS ranges for SNIc/Ib. The total mass of helium left in the star at the end of the simulations, $M_{\rm He}^{\rm env}$ for all our models is presented in Fig. 19. Considering that a SNIc is detected only if

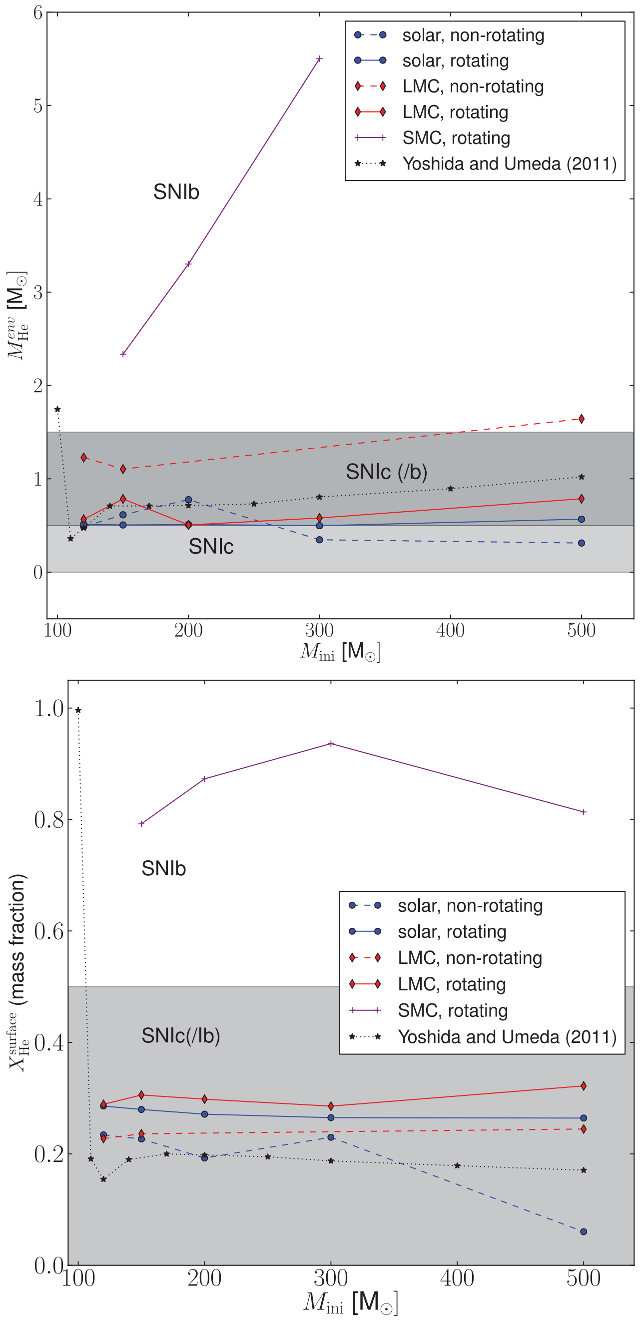

Figure 19. Amount of helium left in the star, $M_{\rm He}^{\rm env}$ (top) and mass fraction of He at the surface, $X_{\rm He}^{\rm surface}$ (bottom) at the end of the simulations.

the total He mass is less than 0.5 M$_\odot$ (light grey area), we see that almost none of our models would predict a SNIc. Only the 300 and 500 non-rotating solar metallicity models would barely qualify. On the other hand, considering that a SNIc is detected if the total He mass is less than 1.5 M$_\odot$ (dark+light grey area), then most models at solar and LMC metallicities would produce SNIc while SMC models would produce SNIb supernova.

A second approach is to use the surface He mass fraction, $X_{\rm He}^{\rm surface}$, since only a shell of material is excited at a given time. We use the value of $X_{\rm He}^{\rm surface} = 0.5$ as in Yoshida & Umeda (2011) and Yoon et al. (2010) as the boundary between SNeIb and SNeIc (see Fig. 19, bottom panel). Using this approach, we find that all our LMC and solar metallicity models end as SNIc, whereas those at SMC metallicity end as SNIb. Since it is mostly the SMC models that are predicted to produce PCSN, our models would predict that PCSN are most likely to appear as SNIb. Yoon et al. (2010) reported that the He lines are not seen in early-time spectra even though the total He mass is as large as 1.0 M$_\odot$ if He is well mixed with CO thus detailed spectral modelling should be used to put tighter constraints on the supernova type.

5.2.1 *Are superluminous SNe PCSNe?*

We have evaluated the initial mass range that might produce PCSN using the final CO core mass of our models. We can now see how our models compare with observed superluminous SNe (SLSNe). Since none of our models retain hydrogen, we will not try to determine a possible initial mass for the progenitor of SNIIn SN 2006gy. Interactions with a dense circumstellar medium is a possible scenario for such SLSNe (Gal-Yam 2012). The case of SN 2007bi is more interesting since this SLSN is a SNIc and its light curve is easily explained by a PCSN (Gal-Yam et al. 2009). The light curve of this supernova can be explained by a PCSN with a CO core mass equal to roughly 100 M$_\odot$. Yoshida & Umeda (2011) calculated models at $Z = 0.004$ (the estimated metallicity for SN 2007bi) and find that models with an initial mass of ∼500 M$_\odot$ end with the required CO core using a standard mass-loss prescription (case A) as shown in Fig. 18. Assuming that SN 2007bi had a SMC metallicity (which is still within uncertainties), we see in Fig. 18 that the desired CO core mass can be obtained from a much lower initial mass range, roughly between 160 and 175 M$_\odot$, which makes the probability of such events much higher.

There are, however, several issues with the PCSN scenario to explain the properties of SN 2007bi. First, all stellar evolution models retain some helium at their surface and it is not clear whether these models would be observed as SNeIc. Secondly, the synthetic spectra from PCSNe seem to be much redder than the observed spectrum of SN 2007bi and other SLSNe (Dessart et al. 2012b, 2013). Other possible scenarios proposed for SLSNe are energetic SNe (see e.g. Yoshida & Umeda 2011) and magnetar-driven explosions (see Dessart et al. 2012b, and references therein).

5.3 GRBs from VMS?

Yoon et al. (2012) calculated a grid of zero-metallicity rotating stars, including the Taylor–Spruit dynamo for the interaction between rotation and magnetic fields. They find that fast rotating stars with an initial mass below about 200 M$_\odot$ retain enough angular momentum in their cores in order to produce a collapsar ($j > j_{\rm Kerr,\, lso}$; Woosley 1993) or a magnetar (see e.g. Wheeler et al. 2000; Burrows et al. 2007; Dessart, O'Connor & Ott 2012c).

The evolution of the surface velocity was described in Section 3.6. Only models at SMC retain a significant amount of rotation during their evolution (see angular momentum contained in the CO core at the end of helium burning in the last column of Table 4) but do they retain enough angular momentum for rotation to affect the fate of the star? The angular momentum profile of the SMC models is presented in Fig. 20. Note that our models do not include the Taylor–Spruit dynamo so represent the most optimistic (highest possible) prediction concerning the angular momentum in the core of these models. Mass loss in the 300 M$_\odot$ model is too strong for the core to retain enough angular momentum for rotation to impact the death of this model. In the 200 M$_\odot$ model, and even more so in the 150 M$_\odot$ model, however, the central part of the

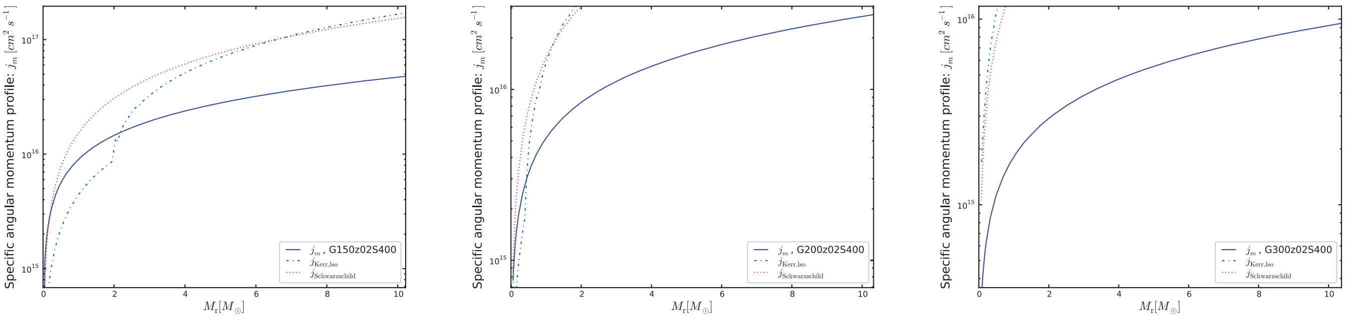

Figure 20. Specific angular momentum profile, $j_{\rm m}$, as a function of the Lagrangian mass coordinate in the core of the SMC rotating 150, 200, 300 $M_\odot$ models, plotted at the end of the calculations (solid line). The dash–dotted line is $j_{\rm Kerr,\,lso} = r_{\rm LSO}\,c$ (Shapiro & Teukolsky 1983, p. 428), where the radius of the last stable orbit, $r_{\rm LSO}$, is given by $r_{\rm ms}$ in formula (12.7.24) from Shapiro & Teukolsky (1983, p. 362) for circular orbit in the Kerr metric. $j_{\rm Kerr,\,lso}$ is the minimum specific angular momentum necessary to form an accretion disc around a rotating BH. $j_{\rm Schwarzschild} = \sqrt{12}Gm/c$ (dotted line) is the minimum specific angular momentum necessary for a non-rotating BH, for reference.

core retain a significant amount of angular momentum that could potentially affect the death of the star. Since the role of rotation is very modest from carbon until just after the end of core silicon burning, even for extremely fast rotators (see e.g. Hirschi, Meynet & Maeder 2005; Chieffi & Limongi 2013), we do not expect rotation to affect significantly the fate of stars that are predicted to explode as PCSN during neon–oxygen burning. However, as discussed in Yoon et al. (2012, and references therein), the large angular momentum content is most interesting for the stars that just fall short of the minimum CO core mass for PCSN (since fast rotation plays an important role during the early collapse; Ott et al. 2004; O'Connor & Ott 2011; Chieffi & Limongi 2013). Indeed, without rotation, these stars would produce a BH following a possible pulsation pair-creation phase, whereas with rotation, these stars could produce energetic asymmetric explosions (GRBs or magnetars). Since the 150 $M_\odot$ model is predicted to explode as a PCSN, we thus do not expect the models presented in this grid to produce GRBs or magnetars but such energetic asymmetric explosions are likely to take place in lower mass and lower metallicity stars (see Hirschi et al. 2005; Yoon & Langer 2005; Woosley & Heger 2006).

6 SUMMARY AND CONCLUSION

We have calculated a grid of stellar models of VMS at SMC, LMC and solar metallicities. Our study is motivated by the finding of VMS including R136a1 (Crowther et al. 2010) and the observation of PCSN candidate, SN 2007bi by Gal-Yam et al. (2009).

The main results of this study are the following.

(i) VMS possess very large convective cores during the MS phase. Typically, in a 200 $M_\odot$ model on the ZAMS the convective core extends over more than 90 per cent of the total mass.

(ii) Even in models with no rotation, due to the importance of the convective core, VMS stars evolve nearly homogeneously.

(iii) Most of the VMS (all at solar Z) remain in blue regions of the HRD and do not go through a luminous blue variable phase.

(iv) They all enter into the WR phase and their typical evolution will be Of-WNL-WNE-WC/WO.

(v) Because of increasing mass-loss rates with the mass, very different initial mass stars end with similar final masses. As a consequence very different initial masses may during some of their evolutionary phases occupy very similar positions in the HRD.

(vi) A significant proportion of the total stellar lifetimes of VMS is spent in the WR phase. At solar metallicity between 16 and 43 per cent depending on the initial mass and rotation. These proportions decrease with the metallicity to values between 12 and 39 per cent for the LMC metallicity.

(vii) A WC star with high Ne (^{20}Ne) and Mg (^{24}Mg) abundances at the surface has necessarily a VMS as progenitor.

(viii) At solar metallicity none of our model is expected to explode as a PCSN. At the metallicity of the LMC, only stars with initial masses above 450 $M_\odot$ for the rotating models and above about 300 $M_\odot$ for the non-rotating case are expected to explode as a PCSN. At the SMC metallicity, the mass range for the PCSN progenitors is much more favourable. We obtain that all rotating stars in the mass range between about 100 and 290 $M_\odot$ would produce PCSNe.

(ix) All the models we have calculated have lost the entire hydrogen-rich layers long before the end of helium burning. Thus our models predict that all VMS stars in the metallicity range studied will produce either a SNIb or SNIc but no SNII.

(x) Assuming that SN 2007bi had a SMC metallicity, we determine an initial mass for the progenitor between 160 and 175 $M_\odot$.

(xi) We do not expect that the models presented in this grid produce GRBs or magnetars. The reason for that is that either they lose too much angular momentum by mass loss or they avoid the formation of a neutron star or BH because they explode as PCSN. Lower mass stars at low metallicities ($Z \lesssim 0.002$), however, may retain enough angular momentum as in metal-free stars (see Chatzopoulos & Wheeler 2012; Yoon et al. 2012) for rotation (and magnetic fields) to play a significant role in their explosion.

To conclude this paper, we can wonder what the importance of the VMS on the scale of galaxies is? Are VMS so rare that whatever their evolution, their impact on energy and mass outputs will anyway be very low? Considering a Salpeter IMF, the number of stars with masses between 120 and 500 $M_\odot$ corresponds to only about 2 per cent of the total number of stars with masses between 8 and 500 $M_\odot$. So they are indeed only very few! On the other hand, one explosion can release a great amount of energy and mass into the ISM. Typically a 200 $M_\odot$ star releases about 10 times more mass than a 20 $M_\odot$ star. If we roughly suppose that for hundred 20 $M_\odot$ stars there are only two 200 $M_\odot$ star, this means that the 200 $M_\odot$ stars contribute to the release of mass at a level corresponding to about 20 per cent of the release of mass by 20 $M_\odot$, which is by far not negligible. Of course this is a rough estimate but, as a rule of thumb, we can say that any quantity released by a VMS ~10-fold intensity compared to that of a typical, 20 $M_\odot$ star will make a non-negligible difference in the overall budget of this quantity at the level of a galaxy. For instance, the high bolometric luminosities, stellar temperatures and mass-loss rates of VMS imply that they will contribute significantly to the radiative and mechanical feedback from stars in high-mass clusters at ages prior to the first SNe (Crowther et al. 2010). Core-collapse SNe produce of the order of $0.05\,\mathrm{M}_{\odot}$ (ejected masses) of iron, $1\,\mathrm{M}_{\odot}$ of each of the α-elements. According to the production factors in table 4 in Heger & Woosley (2002), PCSN produce up to $40\,\mathrm{M}_{\odot}$ of iron, of the order of $30\,\mathrm{M}_{\odot}$ of oxygen and silicon and of the order of $5–10\,\mathrm{M}_{\odot}$ of the other α-elements. Considering that PCSN may occur up to SMC metallicity and represent 2 per cent of SNe at a given metallicity, their contribution to the chemical enrichment of galaxies is significant, especially in the case of iron, oxygen and silicon.

ACKNOWLEDGEMENTS

The authors thank A. Heger and D. Whalen for modelling the evolution of a subset of our models with the KEPLER code and fruitful discussions. They also thank T. Yoshida for supplying the final mass data from the Yoshida & Umeda (2011) paper. NY acknowledges financial support by the Ministry of Higher Education and University of Malaya under Higher Education Academic Training Scheme and the Commonwealth Scholarship Commission for the Split-Site PhD 2010–2011 programme tenable at Keele University. RH acknowledges support from the World Premier International Research Center Initiative (WPI Initiative), MEXT, Japan and from the Eurogenesis EUROCORE programme. The research leading to these results has received funding from the European Research Council under the European Union's Seventh Framework Programme (FP/2007-2013)/ERC Grant Agreement no. 306901. NY and HAK acknowledge support from Fundamental Research Grant Scheme (FRGS/FP009-2012A) under Ministry of Higher Education of Malaysia.

REFERENCES

Abel T., Bryan G. L., Norman M. L., 2002, Sci, 295, 93
Angulo C. et al., 1999, Nucl. Phys. A, 656, 3
Asplund M., Grevesse N., Sauval A. J., 2005, in Barnes T. G., III, Bash F. N., eds, ASP Conf. Ser. Vol. 336, Cosmic Abundances as Records of Stellar Evolution and Nucleosynthesis. Astron. Soc. Pac., San Francisco, p. 25
Bennett M. E. et al., 2012, MNRAS, 420, 3047
Bond J. R., Arnett W. D., Carr B. J., 1984, ApJ, 280, 825
Bromm V., Coppi P. S., Larson R. B., 1999, ApJ, 527, L5
Burrows A., Dessart L., Livne E., Ott C. D., Murphy J., 2007, ApJ, 664, 416
Chatzopoulos E., Wheeler J. C., 2012, ApJ, 748, 42
Chieffi A., Limongi M., 2013, ApJ, 764, 21
Christlieb N. et al., 2002, Nat, 419, 904
Crowther P. A., 2001, in Vanbeveren D., ed., in Astrophysics and Space Science Library, Vol. 264, The Influence of Binaries on Stellar Population Studies. Kluwer, Dordrecht, p . 215
Crowther P. A., Schnurr O., Hirschi R., Yusof N., Parker R. J., Goodwin S. P., Kassim H. A., 2010, MNRAS, 408, 731
Crowther P. A., Hirschi R., Walborn N. R., Yusof N., 2012, in Drissen L., Robert C., St-Louis N., Moffat A., eds, ASP Conf. Ser. Vol. 465, Four Decades of Research on Massive Stars. Astron. Soc. Pac., San Francisco
Cunha K., Hubeny I., Lanz T., 2006, ApJ, 647, L143
de Jager C., Nieuwenhuijzen H., van der Hucht K. A., 1988, A&AS, 72, 259
Dessart L., Hillier D. J., Li C., Woosley S., 2012a, MNRAS, 424, 2139
Dessart L., Hillier D. J., Waldman R., Livne E., Blondin S., 2012b, MNRAS, 426, L76
Dessart L., O'Connor E., Ott C. D., 2012c, ApJ, 754, 76
Dessart L., Waldman R., Livne E., Hillier D. J., Blondin S., 2013, MNRAS, 428, 3227
Eggenberger P., Meynet G., Maeder A., Hirschi R., Charbonnel C., Talon S., Ekström S., 2008, Ap&SS, 316, 43
Ekström S., Meynet G., Chiappini C., Hirschi R., Maeder A., 2008, A&A, 489, 685
Ekström S. et al., 2012, A&A, 537, A146
Eldridge J. J., Vink J. S., 2006, A&A, 452, 295
Eldridge J. J., Izzard R. G., Tout C. A., 2008, MNRAS, 384, 1109
Ferguson J. W., Alexander D. R., Allard F., Barman T., Bodnarik J. G., Hauschildt P. H., Heffner-Wong A., Tamanai A., 2005, ApJ, 623, 585
Figer D. F., 2005, Nat, 434, 192
Frebel A. et al., 2005, Nat, 434, 871
Fryer C. L., Woosley S. E., Heger A., 2001, ApJ, 550, 372
Gal-Yam A., 2012, Sci, 337, 927
Gal-Yam A., Mazzali P., Ofek E. O., 2009, Nat, 462, 624
Georgy C., Meynet G., Walder R., Folini D., Maeder A., 2009, A&A, 502, 611
Georgy C., Ekström S., Meynet G., Massey P., Levesque E. M., Hirschi R., Eggenberger P., Maeder A., 2012, A&A, 542, A29
Gräfener G., Hamann W.-R., 2008, A&A, 482, 945
Gräfener G., Vink J. S., de Koter A., Langer N., 2011, A&A, 535, A56
Greif T. H., Glover S. C. O., Bromm V., Klessen R. S., 2010, ApJ, 716, 510
Hamann W.-R., Gräfener G., Liermann A., 2006, A&A, 457, 1015
Heger A., Woosley S. E., 2002, ApJ, 567, 532
Hirschi R., 2007, A&A, 461, 571
Hirschi R., Meynet G., Maeder A., 2004, A&A, 425, 649
Hirschi R., Meynet G., Maeder A., 2005, A&A, 443, 581
Iglesias C. A., Rogers F. J., 1996, ApJ, 464, 943
Itoh N., Adachi T., Nakagawa M., Kohyama Y., Munakata H., 1989, ApJ, 339, 354
Itoh N., Hayashi H., Nishikawa A., Kohyama Y., 1996, ApJS, 102, 411
Lodders K., 2003, ApJ, 591, 1220
Maeder A., 1997, A&A, 321, 134
Maeder A., Meynet G., 2000a, A&A, 361, 101
Maeder A., Meynet G., 2000b, A&A, 361, 159
Maeder A., Meynet G., 2012, Rev. Mod. Phys., 84, 25
Maeder A., Georgy C., Meynet G., Ekström S., 2012, A&A, 539, A110
Meynet G., Maeder A., 2005, A&A, 429, 581
Muijres L. E., de Koter A., Vink J. S., Krtička J., Kubát J., Langer N., 2011, A&A, 526, A32
Nugis T., Lamers H. J. G. L. M., 2000, A&A, 360, 227
O'Connor E., Ott C. D., 2011, ApJ, 730, 70
Oey M. S., Clarke C. J., 2005, ApJ, 620, L43
Ott C. D., Burrows A., Livne E., Walder R., 2004, ApJ, 600, 834
Salpeter E. E., 1955, ApJ, 121, 161
Sander A., Hamann W.-R., Todt H., 2012, A&A, 540, A144
Shapiro S. L., Teukolsky S. A., 1983, Black Holes, White Dwarfs, and Neutron Stars: The Physics of Compact Objects. Wiley-Interscience, New York
Smith N. et al., 2007, ApJ, 666, 1116
Stacy A., Greif T. H., Bromm V., 2010, MNRAS, 403, 45
Sylvester R. J., Skinner C. J., Barlow M. J., 1998, MNRAS, 301, 1083
Umeda H., Nomoto K., 2002, ApJ, 565, 385
van Loon J. T., Groenewegen M. A. T., de Koter A., Trams N. R., Waters L. B. F. M., Zijlstra A. A., Whitelock P. A., Loup C., 1999, A&A, 351, 559
Vink J. S., de Koter A., Lamers H. J. G. L. M., 2001, A&A, 369, 574
Wellstein S., Langer N., 1999, A&A, 350, 148
Wheeler J. C., Yi I., Höflich P., Wang L., 2000, ApJ, 537, 810
Woosley S. E., 1993, ApJ, 405, 273
Woosley S. E., Heger A., 2006, ApJ, 637, 914
Yoon S.-C., Langer N., 2005, A&A, 443, 643
Yoon S.-C., Woosley S. E., Langer N., 2010, ApJ, 725, 940
Yoon S.-C., Dierks A., Langer N., 2012, A&A, 542, A113
Yoshida T., Umeda H., 2011, MNRAS, 412, L78
Zahn J.-P., 1992, A&A, 265, 115

This paper has been typeset from a TEX/LATEX file prepared by the author.